



저작자표시-비영리-변경금지 2.0 대한민국

이용자는 아래의 조건을 따르는 경우에 한하여 자유롭게

- 이 저작물을 복제, 배포, 전송, 전시, 공연 및 방송할 수 있습니다.

다음과 같은 조건을 따라야 합니다:



저작자표시. 귀하는 원저작자를 표시하여야 합니다.



비영리. 귀하는 이 저작물을 영리 목적으로 이용할 수 없습니다.



변경금지. 귀하는 이 저작물을 개작, 변형 또는 가공할 수 없습니다.

- 귀하는, 이 저작물의 재이용이나 배포의 경우, 이 저작물에 적용된 이용허락조건을 명확하게 나타내어야 합니다.
- 저작권자로부터 별도의 허가를 받으면 이러한 조건들은 적용되지 않습니다.

저작권법에 따른 이용자의 권리는 위의 내용에 의하여 영향을 받지 않습니다.

이것은 [이용허락규약\(Legal Code\)](#)을 이해하기 쉽게 요약한 것입니다.

[Disclaimer](#)

공학박사 학위논문

**Compact three-dimensional displays
based on optical path analysis
in optically transparent medium**

투명한 매질에서의 광 경로 분석을 이용한
집약적 3차원 디스플레이

2017년 2월

서울대학교 대학원

전기컴퓨터공학부

이 창 건

Abstract

Compact three-dimensional displays based on optical path analysis in optically transparent medium

Chang-Kun Lee

Department of Electrical Engineering and Computer Science

College of Engineering

Seoul National University

This dissertation investigates approaches for realizing compact three-dimensional (3D) display systems based on optical path analysis in optically transparent medium. Reducing the physical distance between 3D display apparatuses and an observer is an intuitive method to realize compact 3D display systems. In addition, it is considered compact 3D display systems when they present more 3D data than conventional systems while preserving the size of the systems. For implementing compact 3D display systems with high bandwidth and minimized structure, two optical phenomena are investigated: one is the total internal reflection (TIR) in isotropic materials and the other is the double refraction in birefringent crystals. Both materials are optically transparent in visible range and ray tracing simulations for analyzing the optical path in the materials are performed to apply the unique optical phenomenon into conventional 3D display systems.

An optical light-guide with the TIR is adopted to realize a compact

multi-projection 3D display system. A projection image originated from the projection engine is incident on the optical light-guide and experiences multiple folds by the TIR. The horizontal projection distance of the system is effectively reduced as the thickness of the optical light-guide. After multiple folds, the projection image is emerged from the exit surface of the optical light-guide and collimated to form a viewing zone at the optimum viewing position. The optical path governed by the TIR is analyzed by adopting an equivalent model of the optical light-guide. Through the equivalent model, image distortion for multiple view images in the optical light-guide is evaluated and compensated. For verifying the feasibility of the proposed system, a ten-view multi-projection 3D display system with minimized projection distance is implemented.

To improve the bandwidth of multi-projection 3D display systems and head-mounted display (HMD) systems, a polarization multiplexing technique with the birefringent plate is proposed. With the polarization state of the image and the direction of optic axis of the birefringent plate, the optical path of rays varies in the birefringent material. The optical path switching in the lateral direction is applied in the multi-projection system to duplicate the viewing zone in the lateral direction. Likewise, a multi-focal function in the HMD is realized by adopting the optical path switching in the longitudinal direction. For illuminating the detailed optical path switching and the image characteristic such as an astigmatism and a color dispersion in the birefringent material, ray tracing simulations with the change of optical structure, the optic axis, and wavelengths are performed. By combining the birefringent material and a polarization rotation device, the bandwidth of both the multi-projection

3D display and the HMD is doubled in real-time. Prototypes of both systems are implemented and the feasibility of the proposed systems is verified through experiments.

In this dissertation, the optical phenomena of the TIR and the double refraction realize the compact 3D display systems: the multi-projection 3D display for public and the multi-focal HMD display for individual. The optical components of the optical light-guide and the birefringent plate can be easily combined with the conventional 3D display system and it is expected that the proposed method can contribute to the realization of future 3D display systems with compact size and high bandwidth.

Keywords: Autostereoscopic display, total internal reflection, birefringence, multi-view system, polarization multiplexing, head-mounted display

Student Number: 2013-30254

Contents

Abstract	i
Contents	iv
List of Tables	vi
List of Figures	vii
Chapter 1 Introduction	10
1.1 Overview of modern 3D display providing high quality 3D images	10
1.2 Motivation of this dissertation	15
1.3 Scope and organization	18
Chapter 2 Compact multi-projection 3D displays with optical path analysis of total internal reflection	20
2.1 Introduction	20
2.2 Principle of compact multi-projection 3D display system using optical light-guide	23
2.2.1 Multi-projection 3D display system	23
2.2.2 Optical light-guide for multi-projection 3D display system	26
2.2.3 Analysis on image characteristics of projection images in optical light-guide	34
2.2.4 Pre-distortion method for view image compensation	44
2.3 Implementation of prototype of multi-projection 3D display system with reduced projection distance	47
2.4 Summary and discussion	52
Chapter 3 Compact multi-projection 3D displays with optical path analysis of double refraction	53
3.1 Introduction	53
3.2 Principle of viewing zone duplication in multi-projection 3D display system	57
3.2.1 Polarization-dependent optical path switching in birefringent	

crystal.....	57
3.2.2 Analysis on image formation through birefringent plane-parallel plate	60
3.2.3 Full-color generation of dual projection	64
3.3 Implementation of prototype of viewing zone duplication of multi-projection 3D display system.....	68
3.3.1 Experimental setup for viewing zone duplication of multi-projection 3D display system	68
3.3.2 Luminance distribution measurement of viewing zone duplication of multi-projection 3D display system.....	74
3.4 Summary and discussion	79
Chapter 4 Compact multi-focal 3D HMDs with optical path analysis of double refraction	81
4.1 Introduction	81
4.2 Principle of multi-focal 3D HMD system	86
4.2.1 Multi-focal 3D HMD system using Savart plate	86
4.2.2 Astigmatism compensation by modified Savart plate.....	89
4.2.3 Analysis on lateral chromatic aberration of extraordinary plane.....	96
4.2.4 Additive type compressive light field display	101
4.3 Implementation of prototype of multi-focal 3D HMD system	104
4.4 Summary and discussion	112
Chapter 5 Conclusion	114
Bibliography.....	117
Appendix 129	
초 록 130	

List of Tables

Table 1.1 Pros and cons of multi-projection 3D display and HMD system	15
Table 2.1 Resolution loss of projection images	43
Table 2.2 Experimental conditions for compact multi-projection 3D display system using optical light-guide	48
Table 3.1 Measurement of polarization status of laser diode sources	69
Table 3.2 Experimental conditions for compact multi-projection 3D display system using birefringent plate.....	70
Table 4.1 Simulation conditions for astigmatism analysis in birefringent plate	89
Table 4.2 Simulation conditions for color dispersion analysis in modified Savart plate.....	97
Table 4.3 Experimental conditions for compact multi-focal 3D HMD display system using Savart plate.....	106

List of Figures

Figure 1.1 Scope and organization of this dissertation	19
Figure 2.1 Schematic diagram of (a) multi-view 3D display and (b) multi-projection 3D display (top view)	23
Figure 2.2 Light-guide projection: (a) ray trajectory in wedge-shaped light-guide (side view) and (b) multi-view 3D display system using light-guide (top view)	26
Figure 2.3 Equivalent model of optical light-guide	28
Figure 2.4 Equivalent imaging curve of exit surface	30
Figure 2.5 Locus of equivalent imaging points	33
Figure 2.6 Image transformation in equivalent models: (a) image transformation of reference image and (b) image transformation of pre-distorted image	35
Figure 2.7 Ray tracing of equivalent model: (a) geometry of light-guide, (b) side view, and (c) top view of projector array	38
Figure 2.8 Image estimation results: (a) image at equivalent imaging plane, (b) image at exit surface without total internal reflection, and (c) image at exit surface with total internal reflection	40
Figure 2.9 Active area and common area: (a) overlapped area of active areas and (b) common area	42
Figure 2.10 Resolution degradation in projection image	43
Figure 2.11 Calibrated checkerboard images for each projector	44
Figure 2.12 Overlapped image on the exit surface: (a) before compensation and (b) after compensation	45
Figure 2.13 Experimental setup: (a) schematic diagram of ten-view multi-projection 3D display and (b) prototype of ten-view multi-projection 3D display with optical light-guide	47

Figure 2.14 Overlapped checkerboard pattern at the exit surface: (a) original checkerboard pattern, (b) overlapped image before compensation, (c) overlapped image after compensation, and (d) luminance distribution	49
Figure 2.15 View images of ten-view 3D display: (a) 1st view, (b) 2nd view, (c) 3rd view, (d) 4th view, (e) 5th view, (f) 6th view, (g) 7th view, (h) 8th view, (i) 9th view, and (j) 10th view	51
Figure 3.1 Double refraction in calcite.....	57
Figure 3.2 Concept of viewing zone duplication: (a) dual projection and (b) viewing zone duplication for multi-projection 3D displays	60
Figure 3.3 Lateral displacement in dual projection: (a) lateral displacement with changes in incident angle, (b) projection origin shift in dual projection	62
Figure 3.4 Full-color generation process with temporal multiplexing in dual projection	65
Figure 3.5 Image interweaving process for full-color generation.....	66
Figure 3.6 Experimental setup: (a) prototype of proposed system and (b) duplicated projection origins	68
Figure 3.7 Color conversion by polarization switching	71
Figure 3.8 Leakage in synchronization: (a) mismatch between LC response and display image, and (b) black offset image for leakage reduction	72
Figure 3.9 Series of full-color view images generated by ten-view multi-projection 3D display system	73
Figure 3.10 Luminance measurement setup of prototype	74
Figure 3.11 Luminance distribution of prototype: (a) luminance distribution and crosstalk and (b) normalized luminance distribution	76
Figure 4.1 Schematic diagram of multi-focal 3D HMD system using Savart plate	86

Figure 4.2 Optically equivalent model of multi-focal HMD system using Savart plate.....	87
Figure 4.3 Astigmatism in plane-parallel calcite plate: ray tracing for (a) horizontal component (top view) and (b) vertical component (side view)	90
Figure 4.4 Trajectory of virtual image of point light source with angle of optic axis.....	91
Figure 4.5 Astigmatism compensation using Savart plate with half wave plate: (a) horizontal component (top view) and (b) vertical component (side view).....	93
Figure 4.6 Relationship between focal length of mirror and position of virtual planes: (a) focal length = 45 mm, (b) focal length = 55 mm, (c) focal length = 65 mm, and (d) focal length = 75 mm	95
Figure 4.7 Spectrum of micro OLED and center wavelength, (b) chromatic aberration in modified Savart plate.....	97
Figure 4.8 Chromatic aberration in modified Savart plate	98
Figure 4.9 3D image reconstruction by light field optimization for two additive layers and (b) real-time operation of two additive layers.....	101
Figure 4.10 Real-time operation of two additive layers	103
Figure 4.11 Experimental setup: (a) wearable function of proposed system, (b) detailed configuration of HMD module, and (c) experimental setup with real objects.....	104
Figure 4.12 Focus changes between virtual planes: (a) focus change without compensation and (b) focus change with compensation	107
Figure 4.13 Perspective images in compact 3D HMD system	109
Figure 4.14 Focus changes in compact 3D HMD system	110

Chapter 1 Introduction

1.1 Overview of modern 3D display providing high quality 3D images

Blurring the distinction between a real world scene and a computer-generated virtual world has been the ultimate goal of display field for a long time. State-of-the-art display technologies realize a high density of pixel structures and a large capacity for data processing. In particular, the degree of maturity in two-dimensional (2D) display systems is sufficiently high to provide 2D images with vivid colors of the nature and real-world-like images. Most companies are now able to manufacture high-quality products. However, the market requires a next-generation display device which can change the game, and engineers hope to discover unique properties for pioneering a novel display industry. A three-dimensional (3D) display has long been considered as a promising candidate of the next-generation display.

A basic principle of 3D displays is multiplexing spatial information of 2D display into 2D images with angular information by sacrificing some portion of spatial resolution. Special optical components such as polarization glasses, a lens array, a parallax barrier, and stacked screens act as devices for implementing the multiplexing [1-8]. Since arrangement of 2D image with angular information can reconstruct the 3D image information, it is possible

to induce the depth perception cues of binocular disparity, motion parallax, convergence, and accommodation response [9-12].

Modern 3D displays can be divided into two types with the needs for specially designed wearing aids: a stereoscopic 3D display and an autostereoscopic 3D display. The stereoscopic 3D display is the most popular 3D display system and was first proposed by Wheatstone in the 19th century [13]. A pair of view images for each monocular eye is projected by polarization glasses or a goggle-shaped head-mounted displays (HMDs), and these images are synthesized in the brain. Through the synthesis processing, the observer can experience 3D effects, and this principle is known as the binocular disparity. Because of ease of implementation, the stereoscopic method is successfully commercialized and widely equipped in the theaters, the 3D televisions, and the HMDs [14].

The autostereoscopic 3D display system intuitively generates 3D image information in the space by assigning the directivity into 2D spatial information. Thus, the observer can naturally perceive the 3D images without glasses-type equipment. Many types of autostereoscopic 3D display such as a multi-view, an integral imaging (a light field display), and a volumetric 3D display have been proposed. The multi-view 3D display system spatially distributes view images by combining the 2D display and optical components such as parallax barriers and lenticular lenses. Some of multi-view systems have already been commercialized in the market [15-19]. The integral imaging creates the 3D images by rearranging the set of the 2D information using an array of lens or pinhole. Directional modulation of 2D information by 2D structured array of lenses and pinholes provides quasi-

continuous parallax in the horizontal and the vertical directions [20-25]. The volumetric 3D display is an 3D image reconstruction method in which a volume pixel which is called a voxel scatters light in certain volume space. Rotational or stacked screens are usually implemented as scattering medium for voxels [26-29]. However, the quality of 3D display systems is not as good as that of 2D display systems in current market place. This is because massive amounts of both spatial and angular information are required for reconstructing natural 3D images [25]. The capacity of 3D data is limited in the bandwidth of 2D display devices, and the maximum capacity is inefficient to providing natural parallaxes with high resolution corresponding to the resolution of state-of-the-art 2D display devices. Due to limitations in the image quality and the complexity of the system, the autostereoscopic 3D display is not very attractive to the public as much as a next-generation display system beyond the 2D display and the popularization of the 3D display system has lagged.

Recently, researchers are attracted to the high quality 3D display system with boom of virtual reality (VR) and augmented reality (AR). There are appropriate 3D display systems conforming to this trend. One is a multi-projection system for public 3D display, the other is a HMD system for individual.

The multi-projection 3D display is a kind of spatially multiplexed autostereoscopic displays, and enables massive amounts of spatial and angular data of 3D objects to be provided by stacking projectors in both horizontal and vertical directions. By the virtue of the projection system, it is possible to concentrate the capacity of image information into a single screen

[30-36]. Besides, since each image has inherent directivity according to the orientation of projectors, the spatial and angular resolution can be retained simultaneously. The degree of freedom in scaling of projection image is greater than that of flat panel based 3D display systems. Thus, the technique leads to high-resolution 3D images and improved viewing parameters such as a viewing angle, a depth expression range, and the density of viewpoints [32, 35, 36]. Despite clear 3D image quality, scalability, and fine viewing parameters, the reliability of driving system is quite low, and power and computational errors could be accompanied. Furthermore, the cost issue and the complex system structure act as an obstruction for practical uses. Studies for reducing the physical dimension and improving the bandwidth have been reported in the research field of multi-projection 3D display systems.

Since the HMD system is specialized to have wearable function for individual, it is possible to realize high quality 3D images with a simple optical configuration. Modern HMD systems are comprised of a pair of micro display combined with a single convex lens. The single lens imaging system is designed to realize a large field of view (FOV) for each eye. A pair of images from the micro display is synthesized by the binocular disparity and the observer can be soaked in immersive VR and AR circumstances [37-44]. Though some HMD systems are commercialized in the market, the technology is immature in the field of human factor. For example, it is hard to prevent visual fatigue, which comes from the limited accommodation response at fixed image plane [9-11]. In addition, the absence of consideration in human visual system that the interpupillary distance of human visual system is different to each other can cause depth distortion for

some observers because the binocular images for conventional VR devices are designed to satisfy the average interpupillary distance of 65 mm [45]. For improving the satisfaction of VR and AR experiences, recent progress of wearable display system leans to illuminating the relationship between human depth perception and the HMD system [46-48].

Requirement and desire for high quality 3D display system are quite clear and some candidates have reached the high level of completeness. Further consideration for the physical dimension and the human factor in 3D display system can contribute to leading the next-generation display industry.

1.2 Motivation of this dissertation

Realization of a compact 3D display system based on the multi-projection 3D display and the HMD is in focus of this dissertation. Because of high performance in image quality and viewing characteristics, the multi-projection 3D display system and the HMD system are considered as future public 3D display and mixed reality (MR) apparatus for individuals, respectively. Though both systems have a potential to provide realistic 3D experiences, there are critical issues which block the popularization and the commercialization in current status. In Table 1.1, pros and cons of both systems are presented. Both system shares drawback about bulky system configuration and has some endemic issues according to the principles.

Table 1.1 Pros and cons of multi-projection 3D display and HMD system

	Multi-projection 3D display	Head-mounted display system
Pros	High image quality (= display resolution) Large viewing angle Scalability (= Large size)	High image quality (= display resolution) Immersive 3D experience (= wide field of view) Mixed reality
Cons	Bulky system High cost Low reliability	Bulky system Lack of depth cues Restricted specification

Major issues in the multi-projection system are bulkiness, reliability, and cost. Since the multi-projection 3D display system is comprised of large number of projectors, too much volume and cost are required for implementation and the optical characteristics of each projector can be different to each other [35, 36]. Therefore, it is hard to equip the reliable system in practical uses. In case of the HMD system including the micro display, optical components, and housing, the physical dimension of the system occupies large volume. It is not appropriate for long time uses in entertainments and industrial purposes. Besides, the commercialized HMD products only provide the binocular disparity and observers suffer from the visual fatigue originated by lack of accommodation response [9-11].

If the physical dimension of the multi-projection 3D display system and the HMD systems is reduced or capacity for reconstructing 3D images is improved, it is possible to realize the compact 3D display system and apply those systems to various fields of 3D display. Besides, the improvement of bandwidth in both systems can contribute to assuring the reliable operation with low computational load in the multi-projection 3D display system and relieved the visual fatigue in the HMD display system.

For improving the performance of both systems, many research groups have reported valuable works during the last decade. In the research field of the multi-projection 3D display system, mechanically-operated optical components of a rotating spatial filter, a rotating mirror are widely studied for enlarging the bandwidth of the system [28, 49]. Though the bandwidth of the system is improved, it is hard to accept low reliability of mechanical components in practical uses and the physical dimension of projection area is remained as same as the conventional system. In modern research field of the HMD, the adoption of a multi-focal function in the HMD system is considered as a potential candidate which provides immersive depth experience with the accommodation response [43, 47, 48]. The multi-focal function is usually realized by physically stacking display devices and the

temporal multiplexing of tunable optics such as a liquid lens and a vari-focal optics [50-54]. However, the image quality is degraded by the diffraction limitation in the physical stacking method and optical aberrations in tunable optics method.

In this dissertation, the configuration of the multi-projection 3D display and the HMD system is reconfigured from the point of practical uses with compact form factor. The meaning of the compact 3D display system can be interpreted as follows: reduction in the physical dimension of the systems, and improvement in the bandwidth of display device. Approaches for accomplishing the compact 3D display systems are investigated with combination of optically transparent medium and conventional 3D display systems.

1.3 Scope and organization

This dissertation describes methods for implementing novel compact 3D display systems based on optical path analysis of optically transparent medium such as an isotropic light-guide plate and an birefringent crystal. Two main approaches will be presented: one is reducing the physical dimension of 3D display system by the total internal reflection (TIR), the other is enlarging the bandwidth of 3D display system by the double refraction. Each chapter contains basic concepts and principles of the approaches, and optical ray tracing simulations which illuminate specific parameters and the image characteristics of each system. Prototypes of each system will be presented and the feasibility of the methods will be examined with appropriate experiments. In Chapter 2, a compact multi-projection 3D display system with an optical light-guide will be described. By establishing an optically equivalent model of the optical light-guide, system parameters and image distortion of the system can be investigated. The prototype of a ten-view multi-projection 3D display system with minimized structure will be presented. Chapters 3 and 4 describe a novel polarization multiplexing technique with the birefringent crystal. By illuminating the optical path in birefringent crystal according to variables of a polarization state, an optics axis, an incident angle and wavelengths, a bandwidth-multiplied multi-projection 3D display system and a multi-focal HMD display system can be implemented. In case of the multi-projection 3D display system which distributes multiple viewing zones along the lateral direction, the number of viewing zones can be doubled by applying the birefringent plate which is designed to shift the optical path in the lateral direction. The real-time operation of the bandwidth-multiplied multi-projection 3D display system will be described in Chapter 3. Chapter 4 introduces the multi-focal HMD system with specially designed birefringent optics. By analyzing optical

aberrations of an astigmatism and a color dispersion in a single birefringent plate, well-defined multi-focal image planes will be realized by modification of Savart plate. Unique polarization-dependent chromatic aberration in the birefringent plate will be compensated by sup-pixel based image processing. Along multiple image planes, 3D images for monocular eye can be reconstructed by compressive light field display. The dissertation will be summarized with conclusion in Chapter 5.

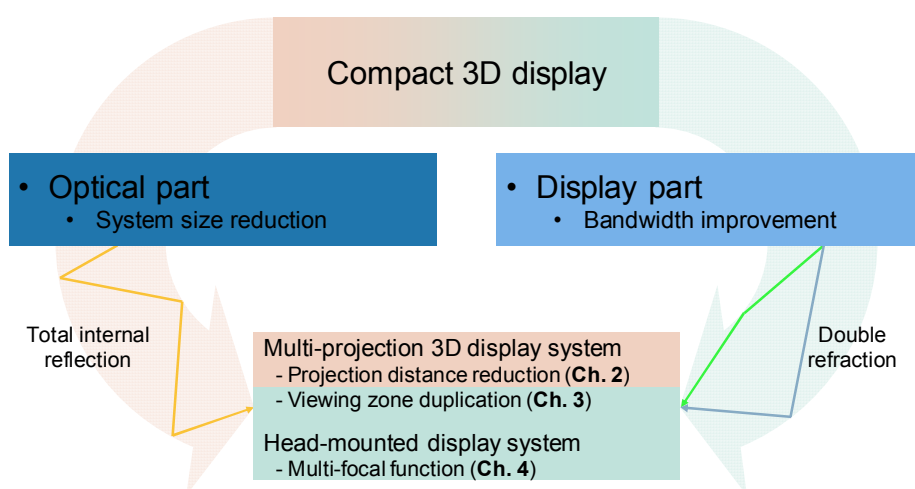


Figure 1.1 Scope and organization of this dissertation

Chapter 2 Compact multi-projection 3D displays with optical path analysis of total internal reflection

2.1 Introduction

The capacity of the original 2D image is limited in the bandwidth of display device, and the maximum capacity is inefficient to providing natural parallax with high resolution corresponding to the resolution of state-of-the-art 2D display device. For overcoming the physical limitation of 2D bandwidth, the concept of multi-projection which stacks multiple projectors in both horizontal and vertical directions was proposed [30, 31]. Since each projection unit is aligned to have different directivity and the resolution of 2D image corresponds to the inherent resolution of projection unit, it is possible to present massive amount of spatio-angular image data. Therefore, the multi-projection 3D display system is appropriate for presenting large-sized 3D images with high resolution and good viewing characteristics.

In spite of high image quality and good viewing characteristics, it is difficult to implement the multi-projection 3D display system for general purposes due to the complex and high-cost of the system including a projector array and associated equipment [35, 36, 55]. In addition, a larger space in both the

horizontal and vertical directions is required compared to a 2D projection system. For reducing the bulky size of the system, short throw projection methods with freeform lens or multiple folding of optical path by optical light-guide projection have been proposed. The performance of the former is good with fine accuracy in imaging. However, the design and manufacturing costs are expensive, and it is difficult to combine multiple projectors and free-form optics [56]. The latter one usually uses the principle of TIR. The optical path of the image is folded in the light-guide, and the effective projection distance is reduced to the thickness of the light-guide [57-63]. The light-guide is composed of an acrylic material, a relatively low cost material. Attempt has been made to realize an autostereoscopic 3D display using light-guide projection [59]. However, the reported system provided only two views with two projectors. Since the two views are fixed, it cannot express natural parallax of 3D objects, which is one of the most important depth cue. The design of the light-guide and the alignment of multiple projectors are complicated, since the geometry of the light-guide needs to be adjusted according to specifications of the projector and the image. In addition, a severe image distortion which degrades the 3D effects occurs according to the incidence condition of the projection images and their orientations [61].

A multi-projection 3D display system with a reduced projection space by adopting the optical light-guide is proposed. For clarifying the image characteristics for multiple view images from each projector, the equivalent model of the optical light-guide is deduced. Through a ray tracing simulation of the equivalent model, the shapes of the image distortion for each view image are estimated, and the distortion in the proposed system is

compensated by image rectification considering an image transformation between the air and the optical light-guide. In the experiment, the prototype of a ten-view multi-projection 3D display system combined with the optical light-guide is used. It is confirmed that the projection distance in horizontal direction is effectively reduced from 266 mm in the conventional system to 48.5 mm. Multiple viewpoints for multi-viewers, and correct view images for achieving 3D effects are realized.

2.2 Principle of compact multi-projection 3D display system using optical light-guide

2.2.1 Multi-projection 3D display system

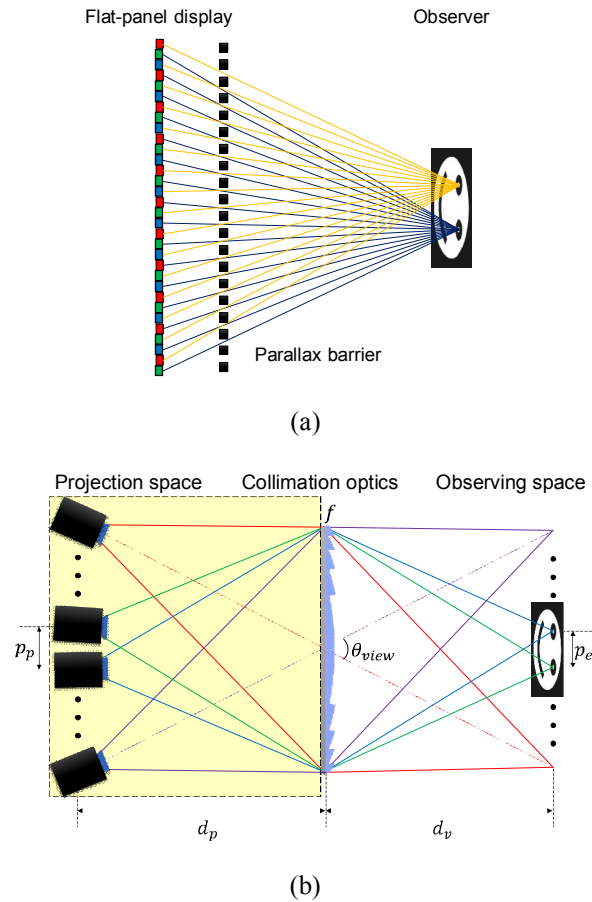


Figure 2.1 Schematic diagram of (a) multi-view 3D display and (b) multi-projection 3D display (top view)

In the flat-panel based multi-view 3D display, 2D image resolution for a

monocular eye is inversely proportional to the number of views because the directivity is assigned for distributing view images on the space by combining lenticular lenses or parallax barriers as shown in Fig. 2.1(a). Therefore, the 3D image that is synthesized by binocular disparity is also degraded with increasing number of views. On the other hand, that in the multi-projection 3D display is conserved because a single projection unit contributes to the formation of a single viewpoint. Since the resolution of the view image is the same as that of the projection unit, the 3D image involving the same resolution is synthesized, as shown in Fig. 2.1(b). Furthermore, it is possible to increase the number of viewpoints and to enhance other viewing parameters by increasing the number of projectors in the lateral direction [30, 55].

Parameters of the system are defined by the geometrical relation. The position of viewpoints, referred to as the optimal viewing position d_v and the interval of viewpoints p_e are calculated by the lens maker's law as follows:

$$d_v = \frac{fd_p}{d_p - f}, \quad (2.1)$$

$$p_e = \frac{p_p d_v}{d_p}, \quad (2.2)$$

where f is the focal length of the collimation lens, d_p is the projection distance between the projector and the collimation lens, and p_p is the interval

of the adjacent projectors which can be adjusted for the interval of viewpoints.

The viewing angle θ_{view} in the multi-projection 3D system is determined by the number of projectors n . The angle between the chief rays of the outermost projectors represents the viewing angle of the system.

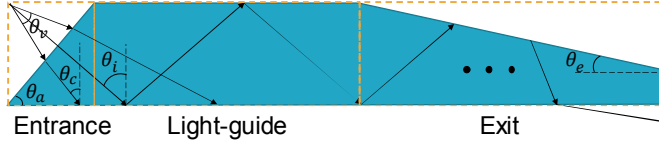
$$\theta_{view} = 2 \tan^{-1} \left(\frac{(n-1)p_p}{2d_p} \right). \quad (2.3)$$

As mentioned above, the large area should be assigned for providing sufficient projection distance, as indicated inside the dashed rectangle in the Fig. 2.1(b). For enlarging the size of image and the number of projectors, larger projection space is required. The required projection space A_p in the air is equal to:

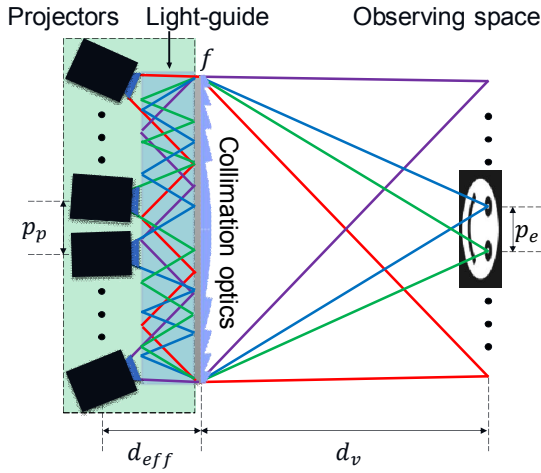
$$A_p = (n-1)p_p d_p. \quad (2.4)$$

From this point of view, the multi-projection 3D display is inefficient to be implemented in general places such as a home, a classroom and an office. For reducing the size of projection space, special optical components for short length projection or densely stacked projection array with a thin projection device are required.

2.2.2 Optical light-guide for multi-projection 3D display system



(a)



(b)

Figure 2.2 Light-guide projection: (a) ray trajectory in wedge-shaped light-guide (side view) and (b) multi-view 3D display system using light-guide (top view)

To reduce the projection distance, Travis et al. proposed the optical light-guide projection system with a shape of wedge prism [57-60]. The optical light-guide has a unique structure composed of three parts: an entrance part, a light-guide part, and an exit part, as shown in Fig. 2.2(a). The angle of

entrance part is determined to satisfy the TIR condition of rays. When the diverging angle of the projector θ_v and the critical angle of the optical light-guide material θ_c are defined, the angle of the entrance part θ_a should satisfy Eq. (2.5) for the TIR of a marginal ray of the projection image.

$$\theta_a \leq \theta_c + \frac{\theta_v'}{2}, \quad (2.5)$$

where θ_v' is the diverging angle in the light-guide which is calculated by Snell's law. If the lower marginal ray satisfies the TIR condition, other rays also experience the TIR, since angles to the normal of other rays at the bottom surface are larger than that of the marginal ray.

After entering the optical light-guide, the ray experiences multiple TIRs until it reaches the exit surface. In the light-guide part, the angle of the ray does not change as the ray propagates, and the projection distance inside the light-guide increases with increasing number of reflections. The angle to the normal of the light-guided ray changes at the exit part because the exit part has a shape of wedge prism with a constant slope. Therefore, the angle to the normal is reduced as the ray undergoes repetitive reflections. The following equation represents the changes in the angle to the normal and the exit condition of the ray in the light-guide.

$$\theta_c \geq \theta_{exit} = \theta_i - 2N\theta_e, \quad (2.6)$$

where θ_{exit} is the angle to the normal of the ray on the bottom interface in the

exit part. θ_i represents the initial incident angle of an arbitrary ray satisfying the TIR condition, and N is the total number of reflections at the inclined surface of the exit part. When the angle to the normal at the exit surface is smaller than the critical angle, the ray can emerge from the light-guide contributing to the representation of images.

By assuming that the optical light-guide is extended over the lateral direction, and projectors are aligned along the entrance part of the optical light-guide, the multi-view images by combining the collimation optics in front of the exit surface can be represented as shown in Fig. 2.2(b). The effective projection distance d_{eff} is reduced in accordance with the thickness of the optical light-guide. Thus, it is possible to implement the multi-projection 3D display with reduced projection space.

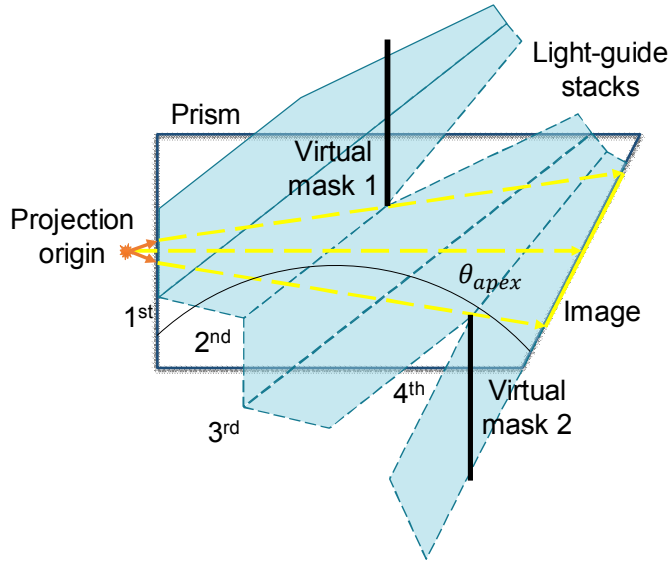


Figure 2.3 Equivalent model of optical light-guide

The ray traveling toward the exit surface of the light-guide is refracted

at the entrance part and experiences multiple TIRs in the optical light-guide part. As the number of reflections in the system increases, the calculation for estimating the trajectory of rays becomes more complex. In addition, the computational load in simulation would be increased in the ray tracing of multiple projectors.

For simplifying the ray tracing for multiple projectors, the equivalent model of the optical light-guide is proposed. For the case of rays transferred by the TIR, the trajectory of rays can be investigated by stacking the optical light-guide at the interfaces [60, 63]. As an example of the trajectory of light-guide stacks, the bundle of rays undergoing four reflections (three reflections in the light-guide part and one reflection in the exit part) in the optical light-guide is depicted in Fig. 2.3. When the TIRs in the light-guide part are converted to the light-guide stacks, the light-guide is approximated to a simple prism structure. The apex angle of the prism θ_{apex} is calculated by angles of the entrance and the exit part, and the number of reflections at the inclined surface in the exit part.

$$\theta_{apex} = \theta_a - 2N\theta_e. \quad (2.7)$$

Detailed specifications of the equivalent prism model can be obtained by calculating the optical path length of the projected rays in the optical light-guide. In addition, the equivalent model provides a hint for suppressing the noise component from the sudden changes in the angle between the light-guide part and the exit part. As shown in the Fig. 2.3, the rays inside

marginal components indicated by dashed rays reach the exit surface without deflections, but rays exceeding the marginal component cannot pass through the stacked light-guide shown in the Fig. 2.3, because the rays are abruptly deflected due to sudden changes in the angle. Unwanted deflections can break the linearity in the image, and noises occur in the image such as overlapping and discontinuity. To reduce noises, the concept of mask blocking the abrupt deflection is adopted in the calculation process of the equivalent prism. The position of masks is calculated by intersecting the marginal ray paths and the corner of the light-guide stack. By combining the equivalent prism and masks, it is possible to simulate the image estimation without noises. Since the ray tracing of the proposed system is simplified, deflections at the light-guide part are replaced by the propagation in the prism. Thus, it is possible to save resources for the image estimation. In addition, the concept of the equivalent model can be expanded over multiple reflection conditions.

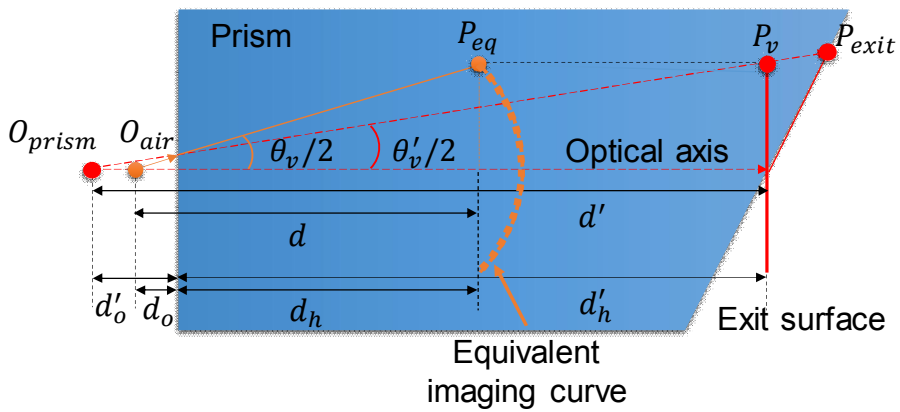


Figure 2.4 Equivalent imaging curve of exit surface

For estimating the image characteristic at the exit surface, the projector should focus on the exit surface. When the projected image is incident on the prism, the image is severely distorted by the refraction because the projection optic is designed to represent the correct image in air. Therefore, the process for correcting the image distortion and adjusting the optimal focus is required.

When the ray (solid line) originated from the projection origin O_{air} with the angle of half of the diverging angle $\theta_v/2$ is incident on the prism, the refracted ray (dashed line) reaches the arbitrary point on the exit surface P_{exit} as shown in Fig. 2.4. The ray will pass through the virtual point P_v on the virtual plane (solid line) which is perpendicular to the optical axis, and is located at the projection distance d_h' from the prism entrance in the horizontal direction. It is assumed that the ray propagating in the air heads toward the virtual point P_{eq} which is located at certain distance d_h in horizontal direction from the prism entrance with the same height of the point P_v . The optical paths of both rays mean that the bundle of rays focused on the point P_{eq} in the air will be focused on the P_v when the light-guide is inserted at the distance d_o from the projection origin in the air. For other points on the virtual plane, the position of P_{eq} can be calculated as the equivalent imaging point. The relationship between these points in the air and the material is defined as follows:

$$d_h \tan\left(\frac{\theta_v}{2}\right) = d_h' \tan\left(\frac{\theta_v'}{2}\right), \quad (2.8)$$

$$d = d_o + d_h = d_o + d_h' \frac{\cos(\theta_v / 2)}{\sqrt{n_l^2 - \sin^2(\theta_v / 2)}}, \quad (2.9)$$

$$d \approx d_o + \frac{d_h'}{n_l} - d_h' \left(\frac{(n_l^2 - 1)}{2n_l^3} \left(\frac{\theta_v}{2} \right)^2 - \frac{(n_l^4 - 10n_l^2 + 9)}{24n_l^5} \left(\frac{\theta_v}{2} \right)^4 + \dots \right), \quad (2.10)$$

$$P_{eq}(x, y) = (d, d \tan(\theta_v / 2)), \quad (2.11)$$

where n_l is the refractive index of the prism material. Since the heights of the virtual points in the air P_{eq} and the prism P_v are equal for both rays, Equation (2.8) which describes the projection distances in the air versus the prism is deduced. From Eq. (2.8), the position of equivalent imaging points in the air for the variation angle of rays can be obtained by Eq. (2.9) in terms of the distance from the projection origin to the light-guide entrance d_o , the optical path in the prism d_h' , and the refractive index of the prism n_l . Equation (2.10) represents Taylor expansion of Eq. (2.9) for the ray with normal incidence. The projection distance in the horizontal direction in the air d can be approximated as the constant value of $d_o + d_h' / n_l$ for paraxial rays.

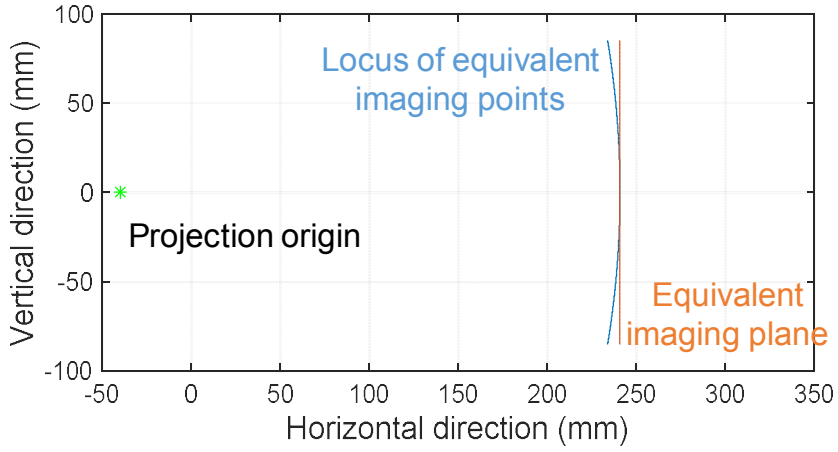


Figure 2.5 Locus of equivalent imaging points

Figure 2.5 shows the locus of equivalent imaging points when the projection origin is located at -40 mm, and the projection distance in the material having the refractive index of 1.49 is 300 mm. The position of equivalent imaging points is calculated using Eq. (2.9) with the condition that the angle to the optical axis of rays changes from -20° to 20° as the curve in the Fig. 2.5. The virtual plane in the material corresponds to the locus of equivalent imaging points in the manner of focus and image information, and the projected image focused on the equivalent imaging plane can be represented on the virtual plane. However, it is difficult to set the projected image on the curved surface, since the projection unit is designed for representing the correct image at a flat surface in the air. For image registration for conventional projector optics, the locus of the equivalent imaging points can be simplified to the plane located at $d_o + d_h'/n_l$ whose value is deduced by Eq. (2.10). Since the conventional projection unit

generally has the maximum diverging angle in the vertical direction of under 20° , the shape of the locus of the equivalent imaging points can be considered as the plane and the approximation therefore is valid for practical uses. The image on the exit surface is also calculated by the projective transformation of the image on the virtual plane. The direct relation between the images at the equivalent imaging plane in the air and the image at the exit surface in the material is revealed. In other words, it is possible to adjust both the focus of the projection unit and the image distortion by applying the concept of the equivalent imaging plane.

2.2.3 Analysis on image characteristics of projection images in optical light-guide

In the case of the multi-projection based 3D display system, projection units are physically separated with different orientations in order to maximize the overlapped region of the images, as shown in the Fig. 2.1(b). However, the image area cannot be matched perfectly. When an inconsistency in the active areas of each projector and the image distortion appears, the observer perceives 3D scenes accompanied by the visual fatigue from the incorrect synthesis of binocular images. For achieving a correct 3D scene that is free from distortions, it is important to address all images into a common area where all projectors can represent the image, and compensate for image distortion [35, 64].

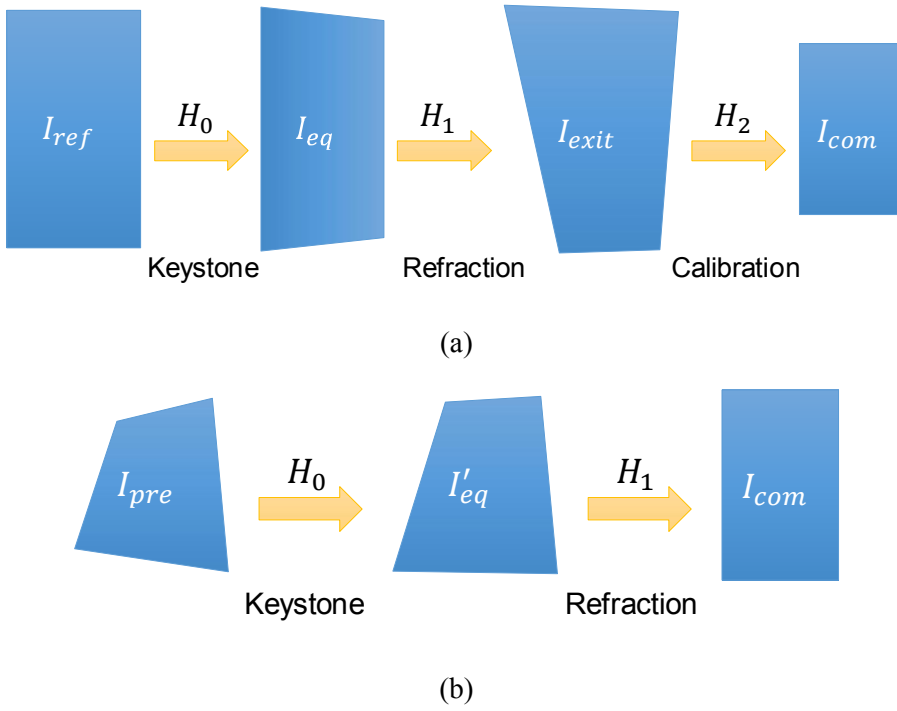


Figure 2.6 Image transformation in equivalent models: (a) image transformation of reference image and (b) image transformation of pre-distorted image

In the conventional multi-projection 3D display system, an auto-calibration method with a capturing device is widely used in order to match the imaging area and for correcting image distortion [35, 65]. However, it is difficult to apply the same method in the proposed system since the distortion originating owing to the refraction in the material must be considered. In the proposed system, two kinds of distortion exist. One is the keystone distortion from the orientation of projectors which also appears in the conventional system. The other one is from the refraction of rays at the

interface between the air and the optical light-guide which is not a factor in the conventional system. The former distortion is simply compensated by projective transformation, while compensating for the latter distortion using the same image transformation is difficult. This is because the refracted angle of rays is governed by Snell's law and the incident angle differs, as a function of the projector orientation. Therefore, the presence of the refractive material makes the ray tracing complicated, and the image analysis which considers the distortion from the refraction is required.

Figure 2.6 shows the image transformation process in the proposed system. The most important issue is to illuminate the degree of distortion between the original image and the distorted area in the material. In the previous section, the equivalent imaging plane so as to directly compare images is defined in the air and in the material. Thus, the image distortion can be compensated by applying the image transformation matrix.

Defining I_{ref} as a reference image at the equivalent imaging plane which corresponds to the input data, it undergoes two distortions and should be modified three times to present the correct image at the common area. The first modification is described as the image transformation H_0 from the reference image to the keystone-distorted image on the equivalent imaging plane. The distorted image by the image transformation H_1 originated by the refraction is then obtained on the exit surface. The last transformation H_2 is setting the distorted image on the exit surface into the common area to correct for the distortion. The transformations of each stage are defined as a 3 by 3 matrix and are calculated by comparing the positions of the four corner points between the original image and the transformed image [66].

The relationship between the reference image I_{ref} and the modified image I_{com} is described as follows:

$$I_{com} = H_2 H_1 H_0 I_{ref}. \quad (2.12)$$

The pre-distorted image is denoted as I_{pre} , which is compensated so as to represent the correct image at the common area, and its image data is provided as input data of the projector, which is also influenced by the keystone effect and the refraction. The correct image will be displayed at the common area after the transformations, and the relationship between the pre-distortion image and the correct image on the common area is defined as

$$I_{com} = H_1 H_0 I_{pre}. \quad (2.13)$$

The transformation matrix between the reference image and the pre-distortion image is calculated by combining Eqs. (2.12) and (2.13) as follows:

$$I_{pre} = H_0^{-1} H_1^{-1} H_2 H_1 H_0 I_{ref}. \quad (2.14)$$

From the specification of each projector and its image distortion data, the transformation matrices of each stage are calculated by Eq. (2.14).

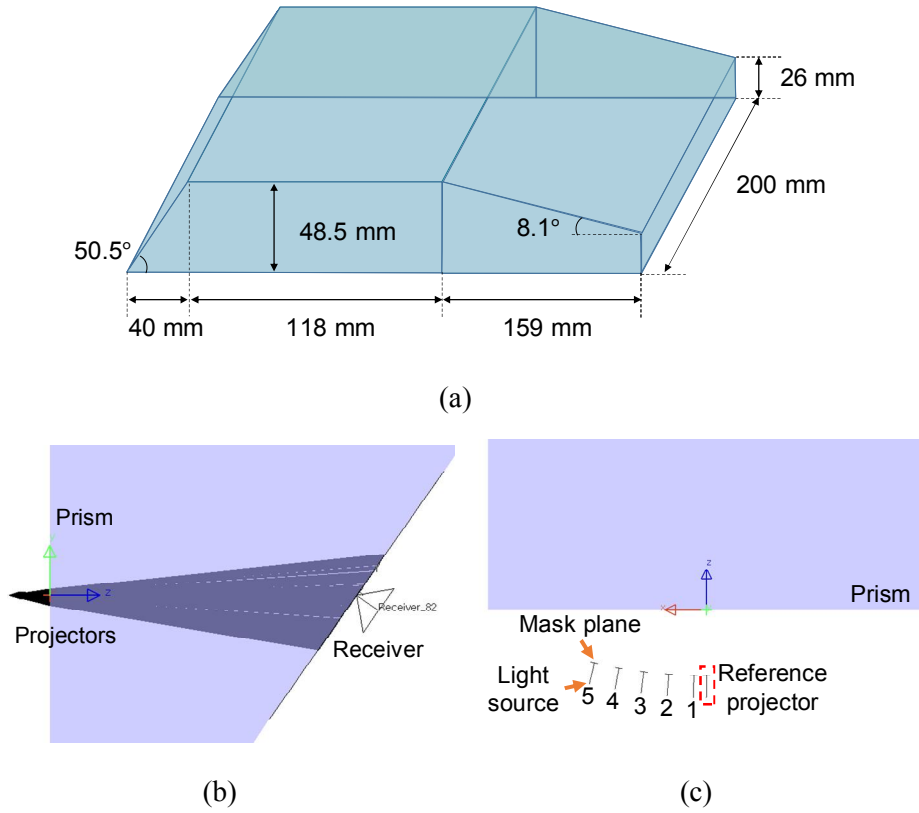
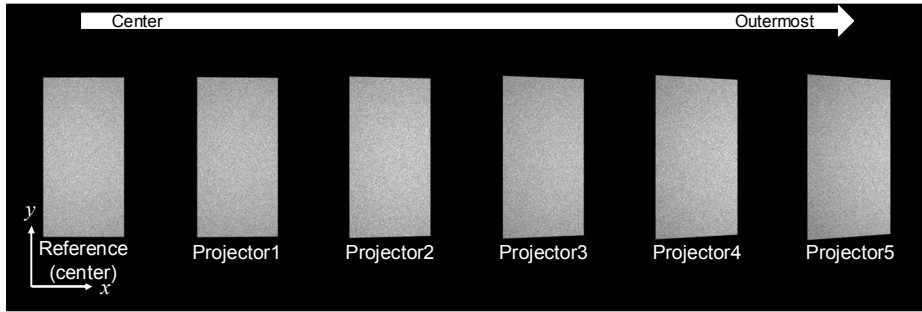


Figure 2.7 Ray tracing of equivalent model: (a) geometry of light-guide, (b) side view, and (c) top view of projector array

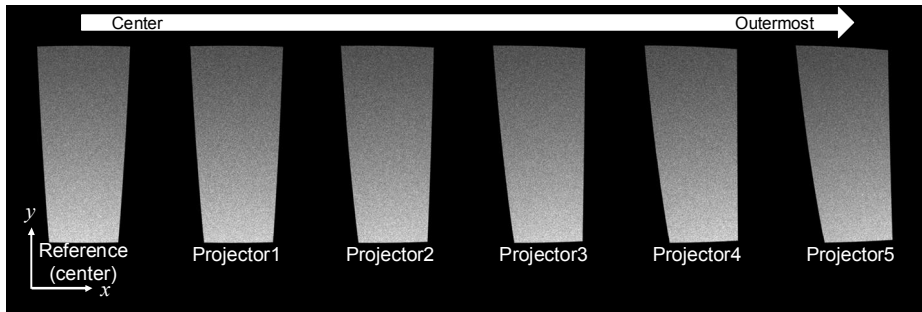
To estimate the change that could occur in images of the proposed system, the ray tracing tool of LightTools 7.3 was adopted. It enables actual parameters of the projector and the material used in the simulation to be determined. The equivalent model of the optical light-guide and the projector array of the proposed system is implemented, and image characteristics at each stage are obtained.

Figure 2.7 shows the captured image of the simulation for constructing

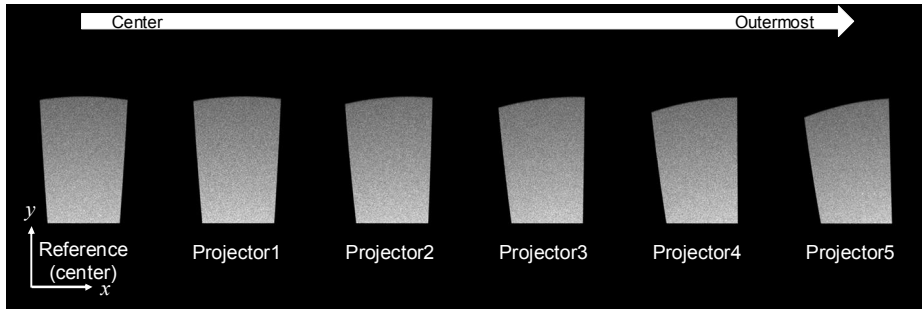
the equivalent model with the projector array. The equivalent model of the optical light-guide was calculated through the actual geometry of the optical light-guide made of acrylic material. The projection unit is modeled as a point light source with the diverging angle corresponding to pico-projectors (Vieway VPL-201, Oriental Electronics, Korea), and the mask plane where input image is inserted. The projector array is comprised of six projectors. Five of them are configured equi-angularly in the positive side from the z -axis and one is used as the reference at the center. Since the configuration of the proposed system is symmetrical with respect to the z -axis, it is possible to estimate the ray tracing results for ten projectors. All projectors are aligned on the arc of a circle with a diameter of 240 mm for the equi-angular configuration. The diameter of the circle is equal to the distance between the projection origin and the equivalent imaging plane. The angular interval between two adjacent projectors is 2.6° . In the ray tracing, 100 million rays are sampled in order to obtain a reliable simulation with the error value of 3.62%.



(a)



(b)



(c)

Figure 2.8 Image estimation results: (a) image at equivalent imaging plane, (b) image at exit surface without total internal reflection, and (c) image at exit surface with total internal reflection

In order to illuminate the transformation matrices and the common area on the exit surface, the degree of image distortion under three different conditions are estimated. Figure 2.8(a) shows the estimated image at the equivalent imaging plane. The reference projector presents a clear image without any distortion, but keystone distortions that become severe when the orientation angle of projector increases can be found. The image transformation matrix of the keystone effect H_0 for each projector is calculated by comparing the reference image and keystone-distorted images. As shown in Fig. 2.8(b), the keystone-distorted image in the Fig. 2.8(a) is distorted more severely by refraction at the interface. To obtain a precise estimation of the distortion, the TIR at the exit surface is ignored in the simulation, since some of the rays satisfying the TIR condition at the exit surface cannot be detected. Likewise, in the simulation results shown in the Fig. 2.8(a), changes in the shape of image become larger as the projector is located far from the center. In addition, the image is elongated in the vertical direction since the optical path of the lower part is shorter than that of the upper part at the exit surface which is inclined with the slope of the apex angle of the prism. The image transformation matrix H_1 is calculated by comparing the keystone-distorted image at the equivalent imaging plane and the distorted image at the exit surface.

Figure 2.8(c) shows the active area of each projector at the exit surface when the TIR is taken into consideration. Since the rays emerging from the optical light-guide can contribute to displaying view images, some parts of the image area in the Fig. 2.8(b) are excluded in the active area. As the oblique angle of the projector increases, the difference in optical paths of

rays corresponding to each corner of the image increases, resulting in additional distortion in the active area of projector.

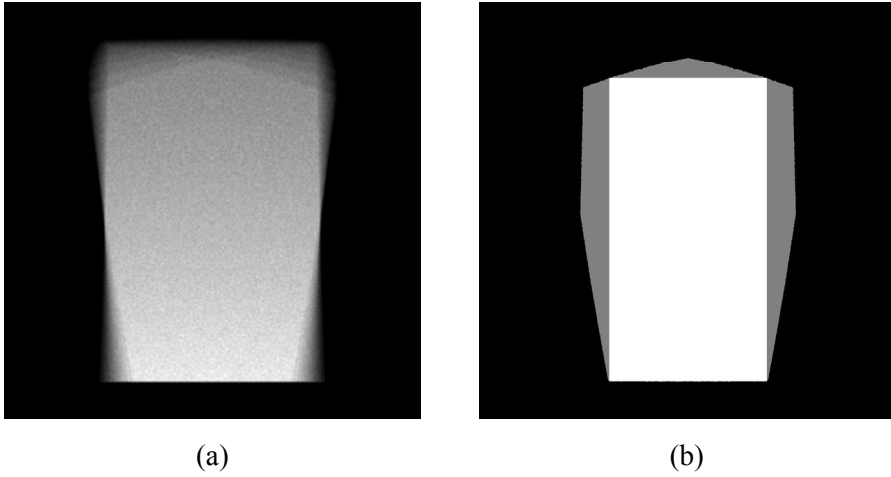


Figure 2.9 Active area and common area: (a) overlapped area of active areas and (b) common area

From the simulation results in the Fig. 2.8(c), it is possible to calculate the common area of the system. When the active areas of ten projectors are overlapped, the image can be represented on the large area, as shown in Fig. 2.9(a). However, all view images should be represented on the common area to permit the image to be shown at the same space on the exit surface as the observing position varies. The area bounded by gray in Fig. 2.9(b) shows the common area of the proposed system calculated by intersecting the active areas.

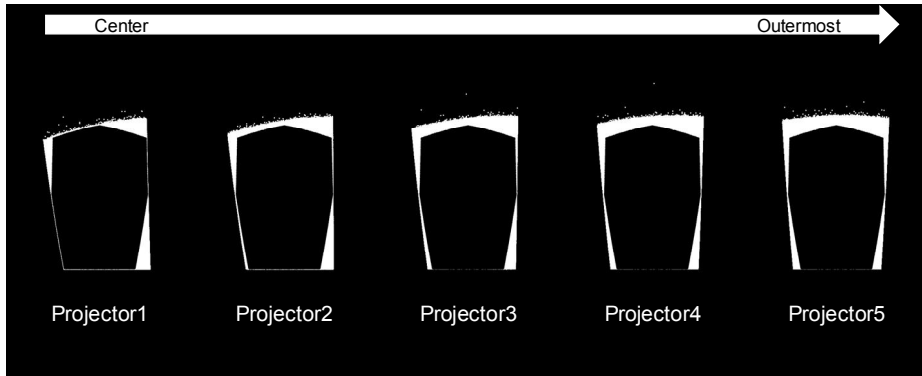


Figure 2.10 Resolution degradation in projection image

Since each projector is aligned with different spatial orientation, projection images cannot be perfectly overlapped and some of pixels cannot contribute to presenting view image in the common area. Figure 2.10 shows the region of projection images which is excluded in the common area. In Table 2.1, resolution losses of each projection image are calculated. The average value of resolution loss in the proposed system is 14.8 %.

Table 2.1 Resolution loss of projection images

	Projector 1	Projector 2	Projector 3	Projector 4	Projector 5
Resolution loss (%)	10.7	13.6	15.6	16.9	17.6

In the image processing for compensation, the common area is restricted to the shape of the rectangle, since the conventional display device and its image sources have the shape of the rectangle. For compensating the distorted image on the exit surface into the common area, the image

transformation matrix H_2 is calculated, and the proposed system provides the correct 3D effects.

2.2.4 Pre-distortion method for view image compensation

From the specifications of each projector and its image distortion data, the transformation matrices of each stage are calculated by Eq. (2.14) and pre-distortion images for each projector are obtained.

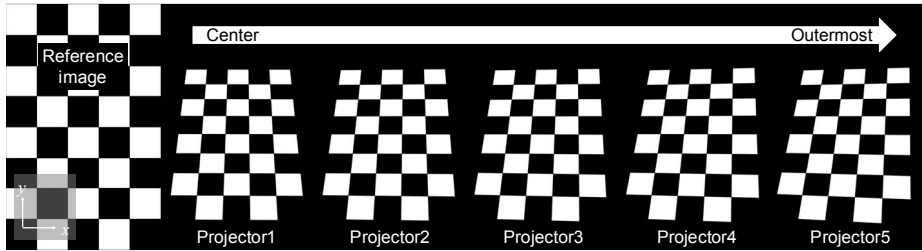


Figure 2.11 Calibrated checkerboard images for each projector

Through the image estimation simulation, the transformation matrices for image compensation are calculated and pre-distorted images are obtained by means of Eq. (2.12). Figure 2.11 shows the series of pre-distorted images originating from the checkerboard image (reference image). Each pre-distorted image will experience the keystone distortion and the refraction. Correct checkerboard images are represented at the common area. To investigate the feasibility of the proposed system, the image simulation with pre-distorted images for ten projectors is performed.

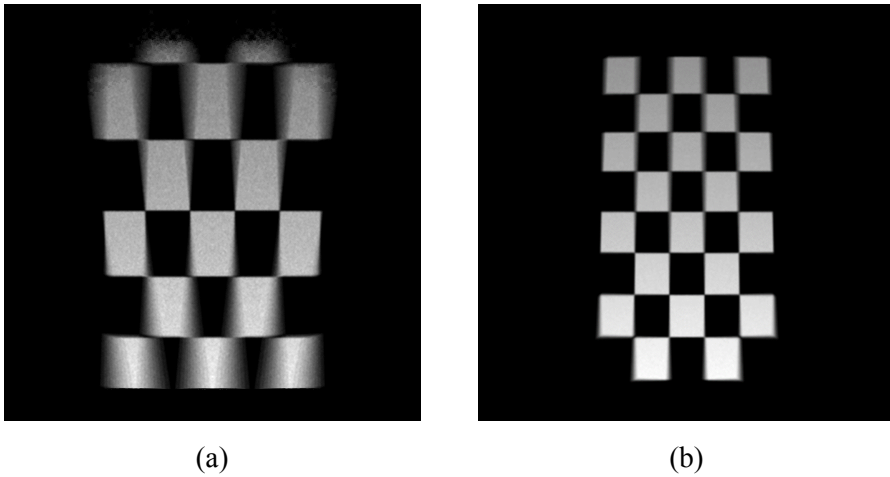


Figure 2.12 Overlapped image on the exit surface: (a) before compensation and (b) after compensation

Figure 2.12 shows the overlapped image on the exit surface when both original and compensated checkerboard patterns are used as input data. Without any compensation in the Fig. 2.12(a), each image from projectors shows severe blurring in the upper and lower parts. In the case of the blurred part, it is difficult to recognize the original images. The entire image size exceeds the common area in the Fig. 2.9(b). These results mean that it is impossible for the observer to perceive correct view images. On the contrary, the clear overlapped checkerboard image appears after the compensation as shown in the Fig. 2.12(b). It is evident that the compensation greatly mitigates the inconsistencies between view images, suggesting that the proposed method provides correct 3D information to multiple viewers.

At the upper and the lower part in the Fig. 2.12(b), there are few blurs and keystone distortions generated by the fact that the equivalent imaging

curve is approximated as the plane in the Fig. 2.5. It is expected that the mismatch can be modified by considering the equivalent imaging curve instead of the plane, and the effect of the mismatch can be ignored when the diverging angle of the projector is as small as specified in Section 2.2.3. The keystone distortion in the Fig. 2.12(b) can be reduced by increasing the number of sampling points in the transformation matrix calculation.

2.3 Implementation of prototype of multi-projection 3D display system with reduced projection distance

To demonstrate the proposed system and the image compensation method, the prototype with ten projectors is implemented as follows.

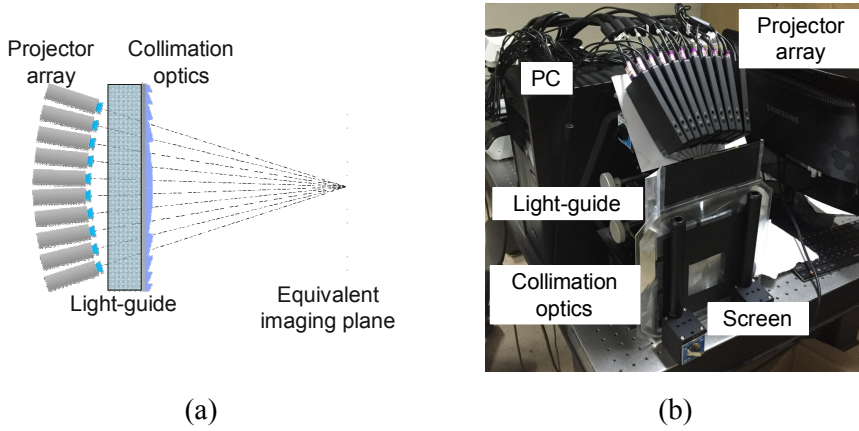


Figure 2.13 Experimental setup: (a) schematic diagram of ten-view multi-projection 3D display and (b) prototype of ten-view multi-projection 3D display with optical light-guide

Figure 2.13(a) shows the schematic diagram of the proposed system. Each projector is aligned toward the center of the equivalent imaging plane with the equi-angular configuration. The focusing plane is adjusted so as to be located at the equivalent imaging plane. After the alignment of the projector array, the light-guide combined with collimation optics is located at the calculated distance from the projection. The experimental setup of the proposed method with ten projectors is implemented as shown in Fig.

2.13(b). Images passing through the optical light-guide by multiple TIRs are collimated toward the viewpoints. As the collimation optics, an anisotropic diffuser having diffusing angles of 60 ° and 1 ° in the vertical and horizontal directions is used for expanding the viewing region in the vertical direction, and a Fresnel lens with the focal length of 200 mm is employed. Detailed specifications of the experimental setup are shown in Table 2.2.

Table 2.2 Experimental conditions for compact multi-projection 3D display system using optical light-guide

Specifications	Values
Interval of projectors	13 mm
Resolution of projectors	960 × 540
Diverging angle of projector	23 ° in vertical direction 19 ° in horizontal direction
Thickness of light-guide	48 mm
Focal length of Fresnel lens	200 mm
Optimal viewing distance	1200 mm
Interval of viewpoints	65 mm
Viewing angle	26 °
Size of common area	110 mm (H) × 65 mm (W)

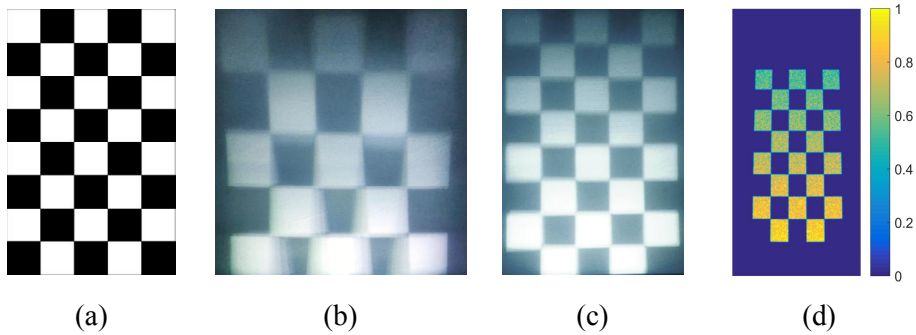


Figure 2.14 Overlapped checkerboard pattern at the exit surface: (a) original checkerboard pattern, (b) overlapped image before compensation, (c) overlapped image after compensation, and (d) luminance distribution

Figure 2.14 shows experimental results for the image compensation. The diffuser is attached on the exit surface to confirm the overlap of correct images at the common area. If the original checkerboard pattern in the Fig. 2.14(a) is inserted as input data, severe blurring at the upper and lower parts occurs as shown in the Fig. 2.14(b) and the image exceeds the common area of the system. In this condition, view images are distorted, and it becomes difficult to synthesize 3D images. Even if the observer perceives the 3D image, the distorted depth and the visual fatigue will be accompanied. When the original images are replaced by pre-distorted images, each image is well overlapped at the common area. The captured image at the diffuser is similar to the original checkerboard pattern, as shown in the Fig. 2.14(c). The size of the common area of the system is 110 mm (H) by 65 mm (W). For representing the same height of the image in the conventional multi-projection 3D display system, the projection distance of 266 mm in the horizontal direction is required when the same projector is implemented. In

the proposed system, the projection distance of 48.5 mm which is the same as the thickness of the light-guide in the horizontal direction is required. The feasibility of image compensation via the equivalent model and the equivalent imaging plane is verified by experimental results. Since the optical path length in the optical light-guide is different in the vertical direction, the uniformity in luminance distribution of image is degraded. As shown in the Fig 2.14(d), the luminance value of the upper side is decreased as 60 % of the lower side. The uniformity issue can be mitigated by weighting the input image.

By combining the optical light-guide and collimation optics, a ten-view 3D display is realized. Every original view image is calibrated through its corresponding transformation matrices calculated by the image estimation method and pre-distorted view images traveling the optical light-guide are focused into the viewpoints. Figure 2.15 shows captured view images of the proposed system at each viewpoint. The view images are represented at the common area and the shape of the original image is conserved with reduced distortion. The view images are clearly separated with the parallax at the optimal viewing distance of 1200 mm.

The experimental results serve to verify that the proposed method provides high resolution perspective images with reduced projection space and the image compensation from the equivalent model of the optical light-guide shows correct view images at the common area.

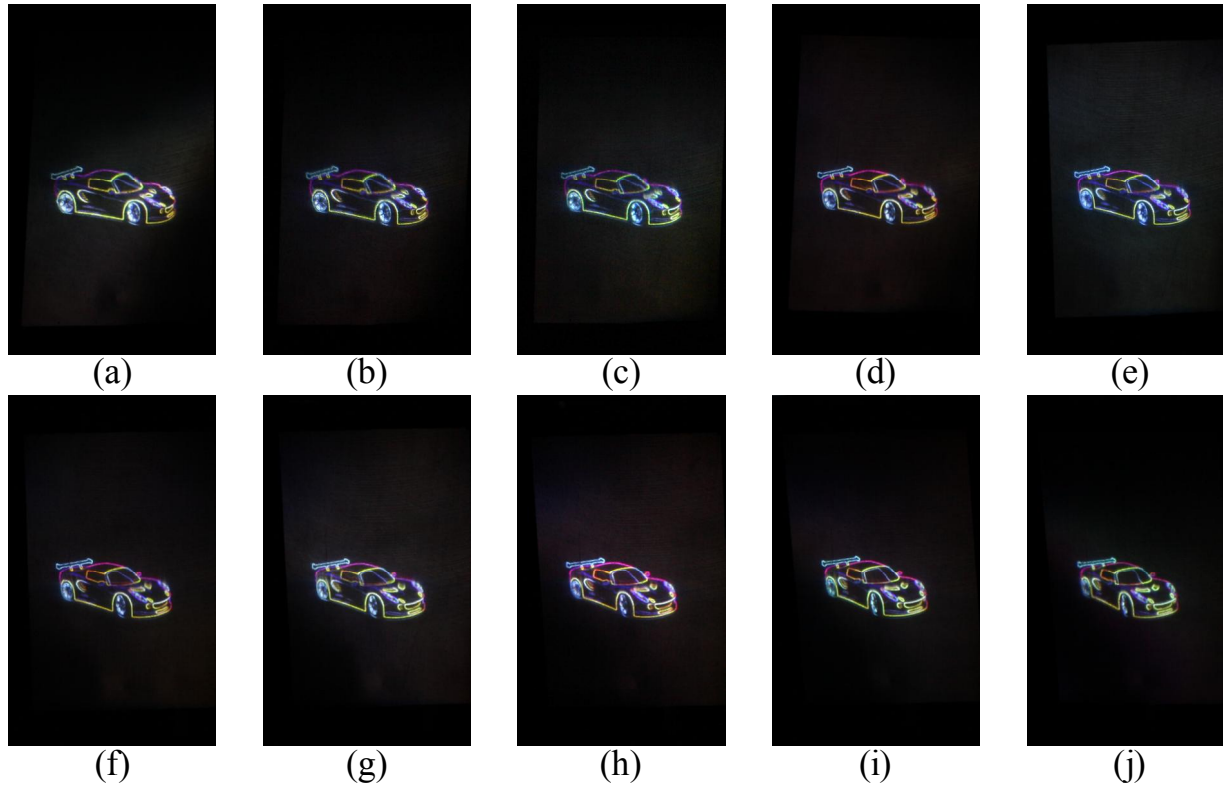


Figure 2.15 View images of ten-view 3D display: (a) 1st view, (b) 2nd view, (c) 3rd view, (d) 4th view, (e) 5th view, (f) 6th view, (g) 7th view, (h) 8th view, (i) 9th view, and (j) 10th view

2.4 Summary and discussion

The multi-projection 3D display system with reduced projection space is proposed by adopting the optical light-guide and its optical equivalent model to permit the system to be manipulated easier. The size of the projection space in the conventional multi-projection 3D display system is reduced by applying the optical light-guide. Through the experiments, it is confirmed that the projection distance of the proposed system is highly reduced by 18% of that of the conventional system for representing the image with the same height, and the viewing zones are finely separated. It is likely that the use of the multi-projection 3D display system with reduced size would help to spread the system into the areas with limited space. In addition, the proposed method is applicable for use in multi-projection 3D displays based on not only multi-view systems but also integral imaging systems, which will widen the choice of 3D display system types. It is expected that the projection distance of the multiple-projector based 3D displays can be reduced more by optimizing the structure of the light-guide and projection optics. For improving the quality of image at the exit surface, optical aberrations and blurring can be modified by implementing projection lens shifting method or laser scanning projection system [33]. Besides, the concept of projection system through the optical light-guide can contribute to implementing compact HMD systems.

Chapter 3 Compact multi-projection 3D displays with optical path analysis of double refraction

3.1 Introduction

In previous chapter, the compact multi-projection 3D display system is proposed by applying the TIR in the optical light-guide. The intuitive method to reduce the projection distance can lead to realization of the compact 3D display system. Besides, improvement in the bandwidth of the system can also contribute to mitigating the complexity and implementing the compact system. In Chapter 3, the method for improving the bandwidth of the multi-projection 3D display system is proposed by applying the double refraction in the birefringent crystal.

High cost for many projectors and complex operating system remain to be solved for popularization of the multi-projection 3D display system. There were techniques reducing the complexity of multiple projectors array, and their operation systems used temporal multiplexing. Jones et al. proposed the 360-degree light field 3D display with the rotation mirror and the digital micromirror device (DMD) projector [36]. The rotation mirror and the DMD projector were synchronized to present correct light field toward reflection direction according to the orientation of rotating mirror. Teng et al.

implemented the super multi-view system with the combination of an array of high resolution micro displays and the rotational filter mask [49]. The optical path of image from micro displays is selectively determined by the time-variable pinhole distribution of rotational filter mask. Takaki et al. fabricated the micro electro mechanical system (MEMS) projection setup, which was specialized for the multi-projection 3D display system with horizontal scanning [67]. The system consists of the mirror galvanometer for horizontal scanning and the MEMS device for presenting gray scale of image. The mirror galvanometer sweeps the image forward angular direction and the 3D images are reconstructed by the collimation optics. The system has the compact size of entire system, but the cost of components such as the mirror galvanometer and the MEMS device is quite expensive, and it is hard to represent the full-color images with three primary colors because there are limitations in modulation speed of image via the MEMS device and the mirror galvanometer. Those methods reconstruct fine 3D images, but the mechanical movement of rotational optical component accompanies safety and reliability issues.

Some researchers reported electrically controllable temporal multiplexing technique without the mechanical movement. By the virtue of the birefringent material, polarization multiplexing of projection-based system can be realized. Akşit et al. proposed a simple method for generating stereoscopic projection system by using projection unit combined with a polarization rotator [68]. By altering the polarization state of image from projector in real-time, the observer wearing polarization glasses sequentially perceives binocular images as the case of stereoscopic television. Recently,

Liu et al. proposed a novel super multi-view 3D display technique by applying a dynamic gating aperture [69]. The position of the aperture is switched in temporal sequence and the multiple viewpoints are effectively generated through each aperture. The system provides good 3D image quality and has small form factor for portable devices, but it is hard to illuminate large screen due to the limitation in brightness of the micro display and multiple sequences.

Park et al. proposed a novel concept of polarization multiplexing technique using the birefringent crystal [70]. According to the polarization states of light, the optical path can be switched when the light passes through the birefringent crystal. By altering the polarization state of elemental image of integral imaging in sequence, two different central depth planes are formed along longitudinal direction, and the depth expression range of integral imaging system is extended. Likewise, the polarization multiplexing technique for the liquid crystal on silicon (LCoS) using the birefringent crystal was proposed. The images from the LCoS could be formed at different positions after passing through the birefringent crystal. The simulation results verify the feasibility of the propose system, but no practical experiments have been performed [71]. Recently, the concept of dual projection, which generates two viewing zones by polarization multiplexing of the projection unit, was proposed by adopting the birefringent crystal [72]. The optical paths of the images from laser scanning projector are split into two different directions after passing through the birefringent crystal. Two separated viewing zones are generated at optimum viewing distance. However, the system just provides view images with single

color channel like anaglyph [73], and it is hard to induce correct binocular disparity with full-color.

The bandwidth improvement in the multi-projection 3D display system is realized by adopting the principle of double refraction in the birefringent crystal. The optical path of image from the projector can be laterally shifted in the birefringent crystal according to the polarization state of light. Since the shifted optical path is considered as the image originated from the projector located in shifted position, the viewing zone can be formed at different viewpoints. Therefore, it is possible to generate two viewing zones separated in the lateral direction using single projection unit. The conventional projection unit has single polarization state for each primary color light source, and it is hard to generate two viewing zones with full-color. For generating the intact view images at both viewing zones generated by single projector, the temporal multiplexing technique with polarization switching is adopted for full-color generation. Since the polarization rotating device and the birefringent crystal are implemented in the proposed system, no mechanical movement and bulky components are required. Through experiments, the feasibility of the proposed method is verified, and the prototype of ten-view multi-projection 3D display with five projectors is implemented. The fine viewing zone duplication is observed, and the full-color view images by temporal multiplexing of polarization state are realized. Furthermore, the luminance distribution of the system is measured for verifying the viewing zone formation.

3.2 Principle of viewing zone duplication in multi-projection 3D display system

3.2.1 Polarization-dependent optical path switching in birefringent crystal

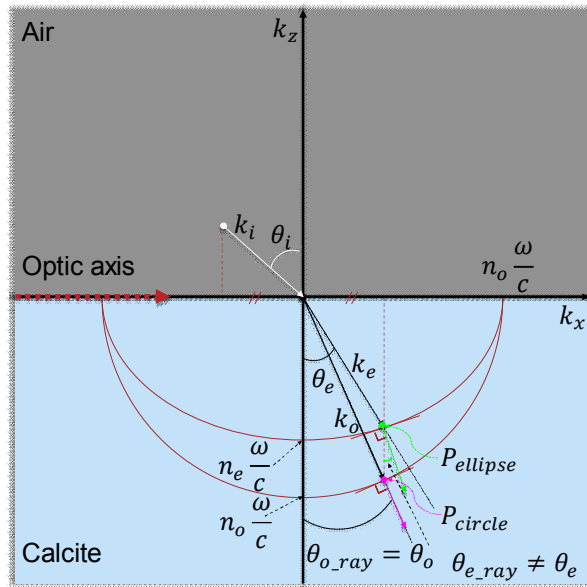


Figure 3.1 Double refraction in calcite

Figure 3.1 shows double refraction in calcite crystal (CaCO_3). The calcite crystal is one of the most popular birefringent crystals widely used in the optical components such as beam splitter, prism, and beam displacer because of its unique properties of birefringence and transparency. The calcite crystal is a negative birefringent crystal: the refractive index of ordinary wave n_o

(=1.658) is greater than that of extraordinary wave n_e (=1.486). The calculation of propagation of wave in the birefringent crystal is based on the boundary condition that all the tangential components of wave vectors along the boundary are same [74]. Since two shells of the normal surface exist in the calcite crystal, there are two possible propagation vectors according to the polarization state of the incident wave. The boundary condition between the air and the birefringent crystal gives following relation:

$$k_i \sin \theta_i = k_o \sin \theta_o = k_e \sin \theta_e, \quad (3.1)$$

where k_i is the magnitude of propagation vector of the incident plane wave with incident angle of θ_i , and k_o and k_e are the magnitudes of propagation vectors of ordinary and extraordinary waves after the refraction, respectively. Those waves are refracted at the boundary with the refraction angle of θ_o and θ_e . In the case of the ordinary wave whose shape of the normal surface shell is a sphere, the wave obeys Snell's law, and the refracted angle and P_{circle} , which is intersection point of the propagation vector and the normal surface shell, are obtained. From the boundary condition in Eq. (3.1), $P_{ellipse}$, where the propagation vector of extraordinary wave and the normal surface shell of the wave with the shape of ellipse intersect, is also calculated by the geometrical operation of ellipsoid as follows:

$$P_{circle} = \left(n_o \frac{\omega}{c} \sin \theta_o, n_o \frac{\omega}{c} \cos \theta_o \right), \quad (3.2)$$

$$P_{ellipse} = \left(n_o \frac{\omega}{c} \sin \theta_o, n_e \frac{\omega}{c} \cos \theta_o \right), \quad (3.3)$$

where ω is the angular frequency of the wave and c is the speed of light. Furthermore, the direction of energy flow which corresponds to the ray direction of extraordinary wave can be obtained. Since the energy flow of the wave is perpendicular to the normal surface, the normal to gradient at $P_{ellipse}$ is equal to the ray direction of θ_{e_ray} :

$$\theta_{e_ray} = \cot \left(\frac{n_o}{n_e} \cot \theta_o \right)^{-1}. \quad (3.4)$$

In case of ordinary wave, the propagation vector and the direction of energy flow coincide due to the sphere-shaped shell of the normal surface. Therefore, there exists difference in ray paths between both waves [75-77]. When the plane-parallel birefringent crystal with optic axis placed along the interface is inclined with the angle of $\theta_{inclined}$ to x -axis and the thickness of the crystal is defined as t , displacement in the lateral direction D between ordinary wave and extraordinary wave is equal to:

$$D = t(\tan \theta_o - \tan \theta_{e_ray}) \cos \theta_{inclined}. \quad (3.5)$$

The trajectory of optical path and the displacement can be modulated by orientation of optic axis as well as incident angle of light. On the other hand, the optical path can be modulated according to purposes.

3.2.2 Analysis on image formation through birefringent plane-parallel plate

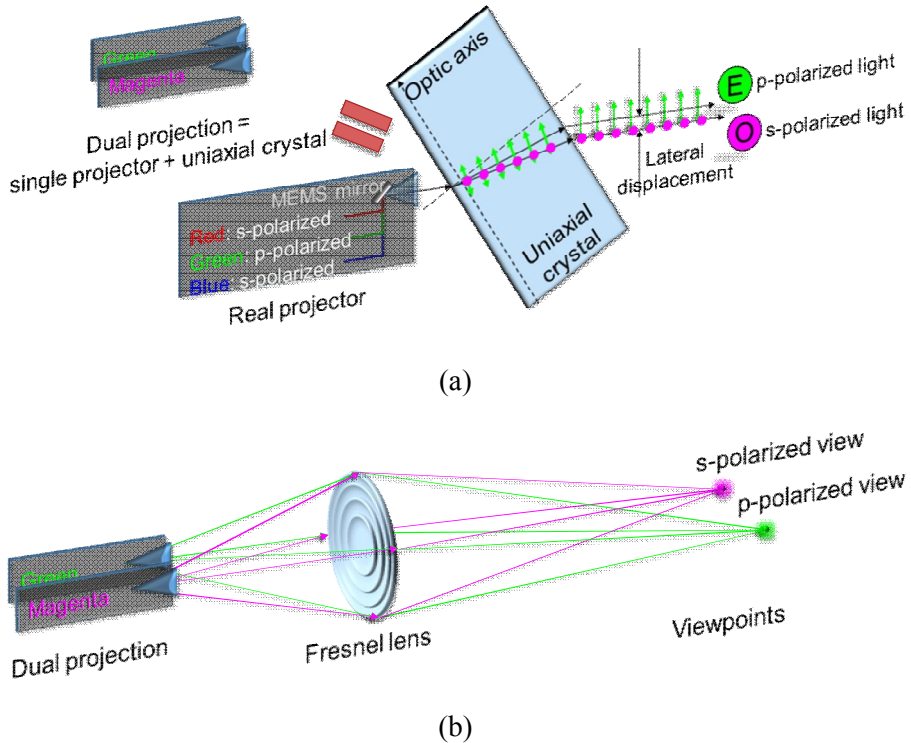
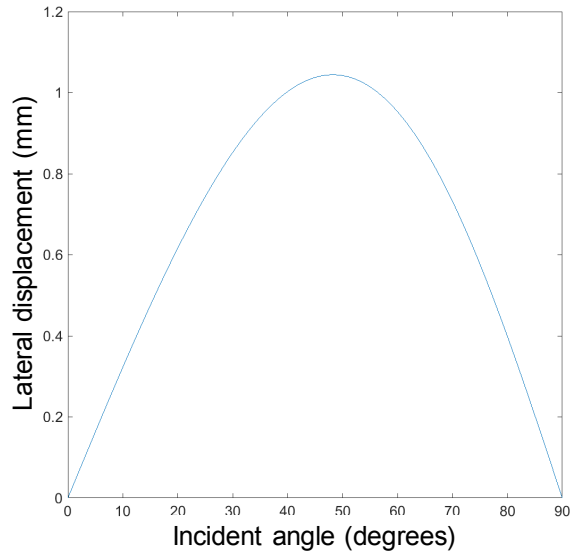


Figure 3.2 Concept of viewing zone duplication: (a) dual projection and (b) viewing zone duplication for multi-projection 3D displays

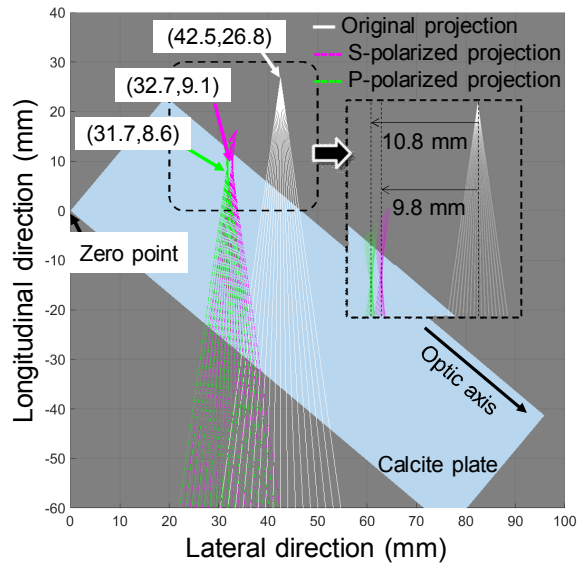
The principle of double refraction can be easily applied to the multi-projection 3D display system, since many projection systems emit the polarized light (e.g. liquid crystal display (LCD) type, LCoS type and laser scanning type). Provided that a laser scanning projector has three primary color sources which are s-polarized (red and blue) and p-polarized (green) respectively, the optical path of lights incident on the birefringent crystal can

be divided into two different trajectories as shown in Fig. 3.2(a). S-polarized red and blue lights pass through the trajectory of ordinary wave, and p-polarized green light traces the path of extraordinary wave. As a result of double refraction, those lights are parallel and propagate into the same direction with the lateral displacement of D . This deviation of optical path can be considered as two spatially separated projectors: one illuminates magenta color and the other illuminates green color. It will be called dual projection system. Furthermore, the image of each viewing zone generated by dual projection can be independently modulated by changing the primary color information of input image. Since two separated projectors can contribute to forming two independent viewpoints at optimum viewing distance, the dual projection system can be adopted in multi-projection 3D display system as shown in Fig. 3.2(b). Two view images originated from separated position would be converged into each viewpoint. It is expected that the series of dual projection system would double the number of viewing zones.

For analyzing the configuration of dual projection system, ray tracing simulations are performed for both polarization states. Figure 3.3(a) shows the relationship between the lateral displacement and the incident angle calculated by the Eq. (3.5) when the optic axis is parallel to the interface, and the thickness of calcite crystal is 30 mm. The maximum lateral displacement is about 1.1 mm near the incident angle of 48° . The lateral displacement could be modulated by tilting the calcite crystal.



(a)



(b)

Figure 3.3 Lateral displacement in dual projection: (a) lateral displacement with changes in incident angle, (b) projection origin shift in dual projection

For illuminating the position of virtual projectors generated by dual projection, the path changes of diverging rays from real projector are traced in the air and the calcite crystal. Then the origins of virtual projectors are retraced in opposite direction of propagation based on the exit position and the propagation angle at the interface. The simulation condition of incident angle is 40° for setting the lateral displacement as 1 mm. In Fig. 3.3(b), white solid lines present the diverging rays from the projection origin of real projector located at 42.5 mm and 26.8 mm in the lateral and the longitudinal direction, when the edge of birefringent crystal is set to zero point. Magenta and green dashed lines present retraced bundle of rays of s- and p-polarized lights, respectively. The retraced rays of s- and p-polarized lights converge onto the narrow spot having the width about $240\ \mu\text{m}$ which is shifted from the real projector position. The spots could be assumed to both s- and p-polarized projection origins. The converging area of s-polarized rays is located at 32.7 mm in the lateral direction and that of p-polarized rays is located at 31.7 mm. The lateral shifts of s- and p-polarized projection origins from the real projector are 9.8 and 10.8 mm, respectively. The location of both origins in the longitudinal direction is near 9 mm, but the projection origin of s-polarized light is a little behind that of p-polarized light. This configuration can affect the longitudinal position or luminance distribution of viewpoints. Since the projection origin shift leads to the image shift at the screen, the image shift is also calculated by the geometrical relationship between the origins. As estimated in the Fig. 3.3(a), it is confirmed that the lateral displacement calculation is valid for diverging rays and virtual projectors generated by dual projection are well separated in the lateral

direction.

Based on the lateral displacement simulation, parameters of the optimum viewing position and the viewpoint interval are calculated in the multi-projection 3D display. The optimum viewing position of d_v is calculated by the lens maker's law and the interval of viewpoints p_{dual} is determined by distance relationship between lens and projection origin:

$$\frac{1}{d_p} + \frac{1}{d_v} = \frac{1}{f_{Fresnel}}, \quad (3.6)$$

$$p_{dual} = D \frac{d_v}{d_p}, \quad (3.7)$$

where d_p is the distance between projection origin and Fresnel lens, and f is the focal length of Fresnel lens. The interval of viewpoints generated by dual projection is calculated by the magnification of the system.

Consequently, it is possible to increase the viewing zones effectively, and the density of viewing zone can be increased or the system load can be reduced to the half of the conventional system.

3.2.3 Full-color generation of dual projection

As shown in the Fig. 3.2(b), the p-polarized viewing zones are lack of green color and the s-polarized viewing zones present only green color. This configuration is similar to the anaglyph – one of the early stereoscopic 3D display technology, which provides binocular disparity by means of the color

filtering glasses [73]. Since lack of color information for monocular eye cannot induce perfect 3D image perception, there were attempts to switch colors in the anaglyph by using temporal multiplexing [68, 73]. Likewise, it is possible to generate full-color 3D images in the proposed method by polarization multiplexing technique.

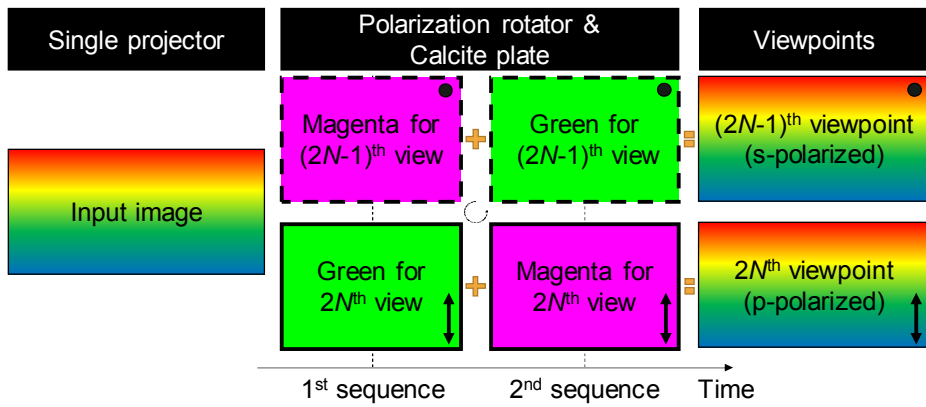


Figure 3.4 Full-color generation process with temporal multiplexing in dual projection

The basic principle of the full-color representation in the display device is controlling the gray level of three primary colors: red, green, and blue. Therefore, sequential switching of colors enables the system to generate the full-color in the proposed method. Figure 3.4 shows the schematic diagram of polarization-based temporal multiplexing for full-color generation. In case of the system, the color of viewpoints will be switched by altering the polarization states of magenta and green images with 90° rotations of its vibration axis. The LCD acts as the polarization rotation, and it is easy to

implement the polarization switching by changing the voltage of the LCD device. In the first sequence for the N^{th} real projector without any polarization modulation, the s-polarized magenta image and the p-polarized green image are presented onto the $(2N-1)^{\text{th}}$ and $2N^{\text{th}}$ viewpoints, respectively. Then, the LCD rotates the polarization of both images by 90° , and the optical paths of images are switched in the second sequence. When the switching speed of the polarization is as fast as the critical flicker fusion frequency so that human cannot perceive the changes in both sequences, the magenta and green images are adequately synthesized, and the observer will perceive the full-color view images at each viewing zone.

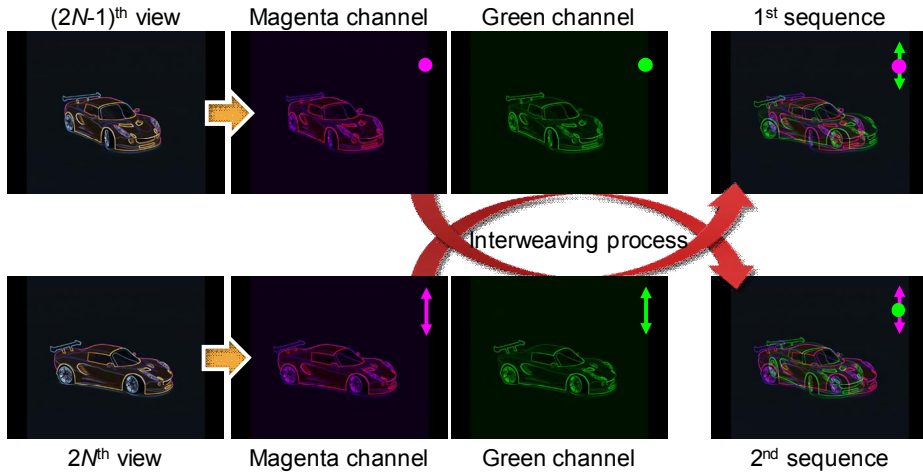


Figure 3.5 Image interweaving process for full-color generation

Figure 3.5 shows the interweaving process of two adjacent view images for full-color generation. Since the input image for real projector contributes to representing two adjacent view images, the input image should include

both adjacent view images. Assuming the magenta view image is formed at $(2N-1)^{\text{th}}$ viewpoint, and the green view image is formed at $2N^{\text{th}}$ viewpoint in the first sequence, the input image should be modulated for representing the correct view information simultaneously. Therefore, the magenta $(2N-1)^{\text{th}}$ view image and the green $2N^{\text{th}}$ view image are interweaved as the first sequence input image for N^{th} real projector. Synthesized view image will be divided into both $(2N-1)^{\text{th}}$ and $2N^{\text{th}}$ view images, respectively. Thus, the second sequence is generated by interweaving the magenta $2N^{\text{th}}$ view information with the green $(2N-1)^{\text{th}}$ view information. Consequentially, the s-polarized $(2N-1)^{\text{th}}$ view image and the p-polarized $2N^{\text{th}}$ view image will be observed at corresponding viewpoints with the full-color. With the changes in sequence, the input voltage of LCD device should be synchronized for rotating the polarization states of input images.

3.3 Implementation of prototype of viewing zone duplication of multi-projection 3D display system

3.3.1 Experimental setup for viewing zone duplication of multi-projection 3D display system

The prototype of ten-view multi-projection 3D display system applying dual projection is implemented for illuminating the feasibility of the proposed system. Moreover, luminance distribution measurement of the proposed system is performed with the changes in polarization states in each sequence.

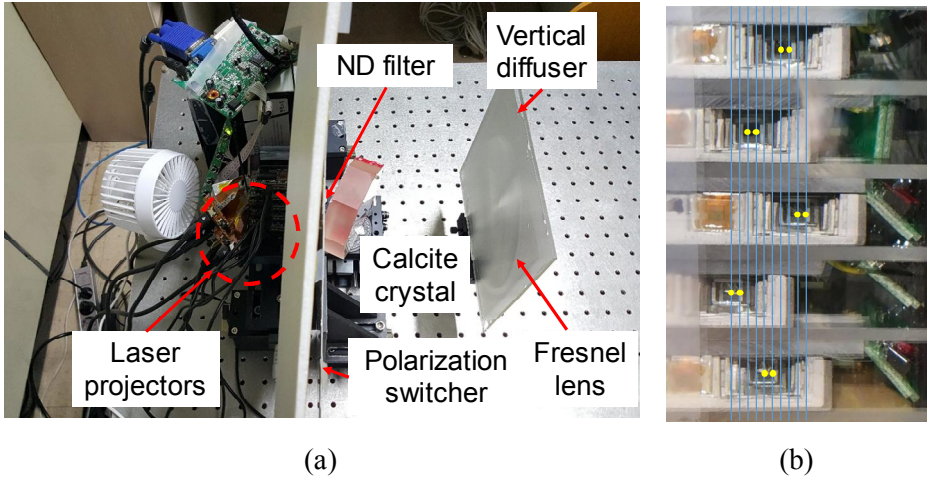


Figure 3.6 Experimental setup: (a) prototype of proposed system and (b) duplicated projection origins

Figure 3.6(a) shows the experimental setup of ten-view multi-projection 3D display system with five laser scanning projectors, the LCD as the

polarization rotator, the calcite crystal as birefringent crystal, and collimation optics. The laser scanning projectors (MicroVision, SHOWWXTM, USA) are stacked in vertical direction, and the horizontal position of each projector is set to maintain the uniform gap between adjacent projectors. The projector array and polarization switcher of polarizer-detached LCD (ODHitec, OD121S1LG-TAS, Korea) is synchronized for the full-color generation. For aligning the polarization axis of laser scanning projector and polarization rotator, the polarization states of laser diode sources in the laser scanning projector are measured by the polarimeter (Thorlabs, PAX7510IR1-T), and the detailed polarization information of each source is shown in Table 3.1.

Table 3.1 Measurement of polarization status of laser diode sources

Specifications	Polarization information		
Wavelengths of laser sources	642 nm (Red)	532 nm (Green)	442 nm (Blue)
Azimuthal angle	40.19 °	-41.78 °	44.45 °
Ellipticity	9.89	0.66	9.96

The calcite crystal is inclined with the angle of 40 ° for duplicating projectors with uniform separation distance. The inclined angle of the calcite plate is calculated by the Eq. (3.5) for the condition that the lateral displacement is 1 mm. The points indicated in the Fig. 3.6(b) correspond to projection origins of the proposed system, and it is confirmed that ten virtual projectors are generated by five real projectors with the calcite crystal.

Neutral density filter having transmittance of 0.391% is inserted in front of projector array for protecting eyes and sensors. The anisotropic diffuser expands the viewing region in the vertical direction, and the Fresnel lens of 150 mm focal length is located at 170 mm from the projection origin to form the viewing zone at the optimum viewing distance. The detailed experimental conditions are shown in Table 3.2.

Table 3.2 Experimental conditions for compact multi-projection 3D display system using birefringent plate

Specifications	Values
Interval of real projectors	2 mm
Interval of projection origins	1 mm
Resolution of projectors	848 × 480
Optic axis of calcite crystal	Along with interface
Dimension of calcite crystal	100 mm (W) × 100 mm (H) × 30 mm (D)
Diffusing angle of anisotropic diffuser	40 ° in vertical direction 0.2 ° in horizontal direction
Focal length of Fresnel lens	150 mm
Distance between virtual projector and Fresnel lens	170 mm
Optimal viewing distance	1275 mm
Interval of viewpoints	7 mm

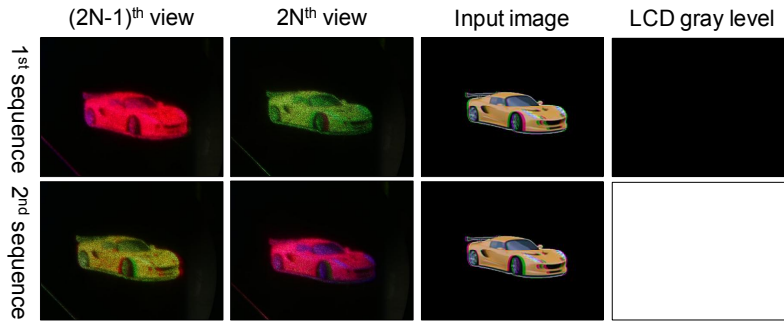


Figure 3.7 Color conversion by polarization switching

Figure 3.7 shows the color conversion of the proposed system. When the polarization states are switched by changing the gray level of the LCD polarization rotator, the color of view images is also switched simultaneously. The color balance of each viewpoint is not uniform because the azimuthal angles of polarization of red and blue sources are slightly different, and the polarization axes of magenta (red and blue) and green sources are not perfectly orthogonal as indicated in the Table 3.1. In addition, leakages from the ellipticity of red and blue sources act as noises at each viewpoint. Though the color uniformity of both sequences is low, the color conversion in multiplexing process is verified. The uniformity can be improved by modulating the polarization state of each source to have well-defined linear polarization and geometry of the sources to have parallel or orthogonal relationship. When the fast switching of input sources for projector and polarization rotator is realized, the magenta and green images are synthesized, and the observer perceives the full-color view images. Visualization of polarization switching and temporal multiplexing for full-color generation is provided in the Fig. 3.7. The cycle of temporal

multiplexing is $1/15$ s. Since the response time of LC polarization rotator is slower than the image switching speed of laser scanning projector, in Fig. 3.8(a), there is leakage between each sequence. For reducing the leakage, black offset images are inserted between adjacent sequences as shown in Fig. 3.8(b). The noises originated from the slow rising and falling time of LC response can be also minimized by adopting the fast polarization switching devices such as ferroelectric LC.

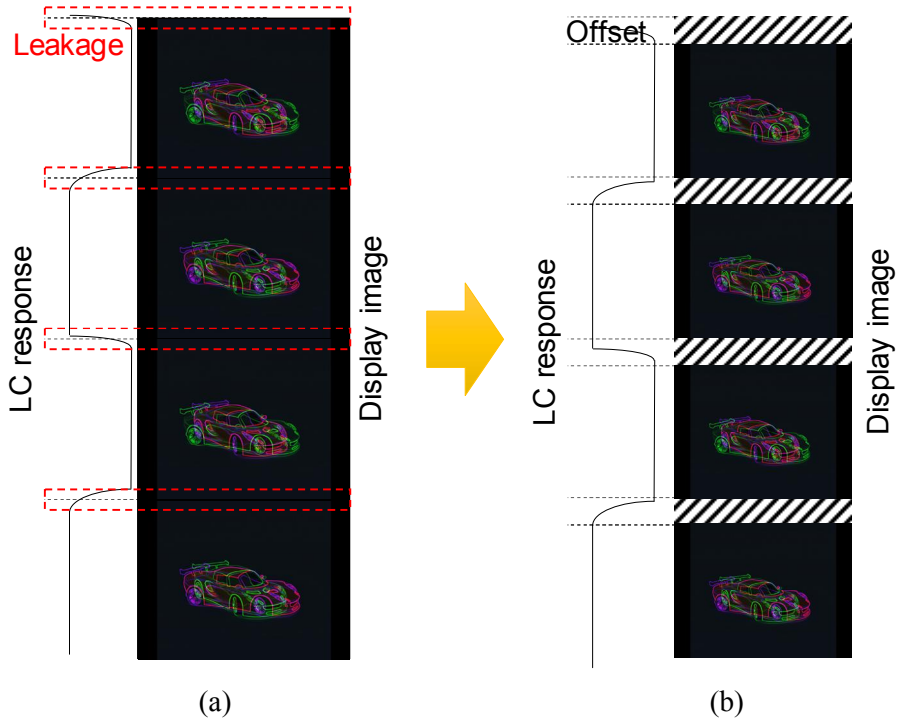


Figure 3.8 Leakage in synchronization: (a) mismatch between LC response and display image, and (b) black offset image for leakage reduction

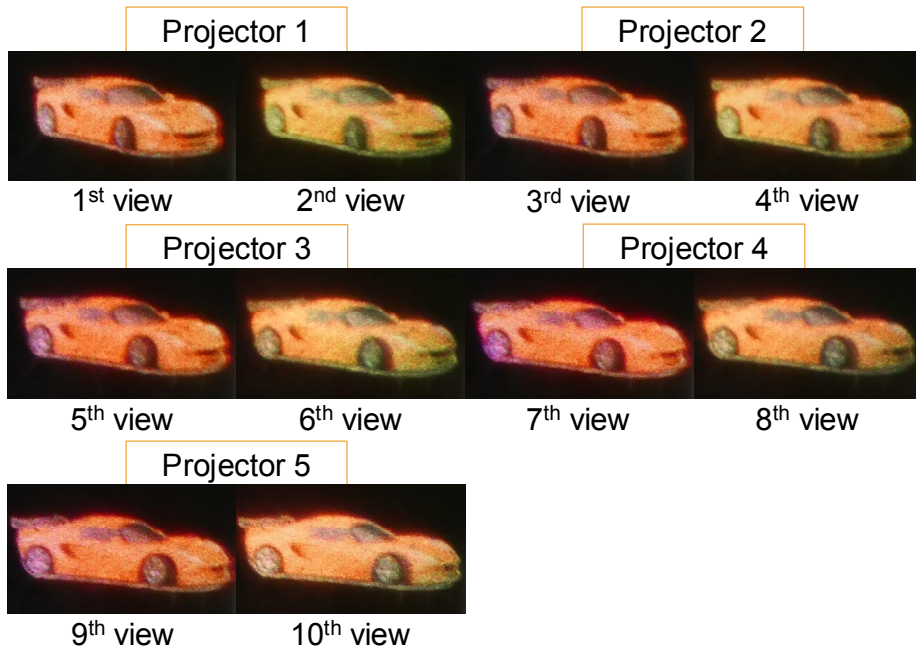


Figure 3.9 Series of full-color view images generated by ten-view multi-projection 3D display system

By combining the five laser projectors and the polarization rotator, the viewing zone duplicated ten-view multi-projection 3D display is realized. Figure 3.9 shows the series of captured view images generated by the prototype. The prototype is operated with 15 frames per second, and the view images are captured at optimum viewing distance of 1275 mm during 1/8 s of shutter speed. The interval of capturing corresponds to the interval of viewpoints of 7 mm. The view images are clearly separated with the parallax. As mentioned earlier, though the odd-numbered (s-polarized) images are reddish and the even-numbered (p-polarized) are greenish because of the noise from the inherent source property, the sequential images are

synthesized, and the full-color images are observed at every viewpoint in real-time. The quality of the images is affected by the low resolution of projectors, the laser speckle from laser diode sources, and the diffraction from the pixelated structure of polarization rotator of LCD. The high resolution projector with speckle reduction and diffraction-free polarization rotator will improve the image quality. The results verify the feasibility of dual projection and full-color generation by polarization switching.

3.3.2 Luminance distribution measurement of viewing zone duplication of multi-projection 3D display system

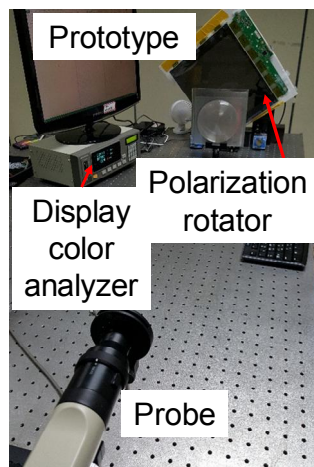


Figure 3.10 Luminance measurement setup of prototype

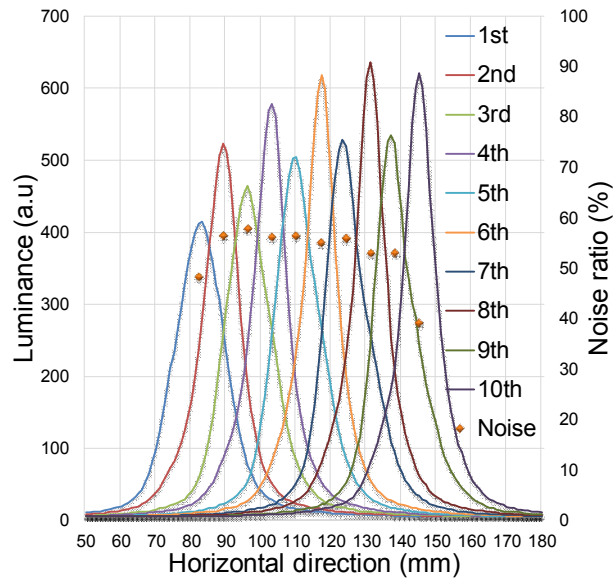
For analyzing viewing parameters such as the viewpoint interval and the noise, the luminance distribution of viewpoints is measured in the horizontal direction [78, 79]. Figure 3.10 shows the luminance measurement setup of the prototype. The display color analyzer (Konica Minolta, CA-210, Japan)

with 1 mm aperture is implemented for measuring the luminance distribution at the calculated optimum viewing position. The range of the measurement is from 50 mm to 180 mm with the sampling interval of 1 mm in horizontal direction. Since the full-color viewpoint is generated by switching of colors in the proposed method, two-step measurement is adopted for each sequence and the luminance values of each step are added for obtaining the luminance distribution at each viewpoint as follows:

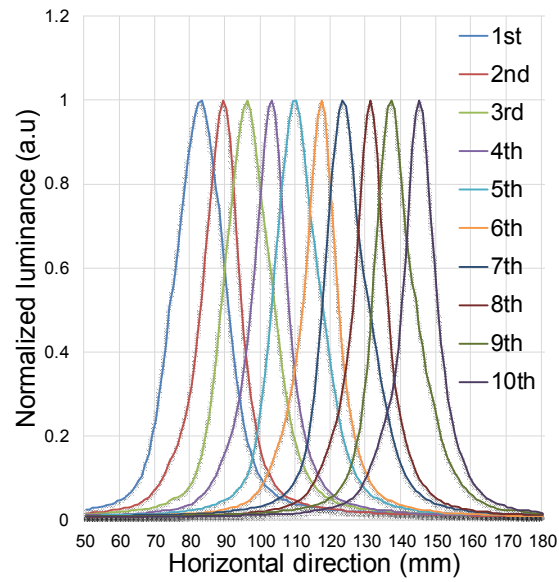
$$L_n = L_{n_1st} + L_{n_2nd}, \quad (3.8)$$

where L_{n_1st} and L_{n_2nd} are the luminance values of the first and the second sequence of n^{th} viewpoint, respectively. The L_n is the peak luminance value of n^{th} viewpoint. When the total number of viewpoints and the measured total luminance at n^{th} viewpoint are defined as P and L_{n_total} , the noise to total luminance ratio C_n at the n^{th} viewpoint is calculated by comparing the peak luminance value of corresponding viewing zone and the summation of luminance values from unintended viewing zone as follows:

$$C_n = \sum_{\substack{i=1 \\ i \neq n}}^P L_i \bigg/ L_{n_total} \times 100(\%). \quad (3.9)$$



(a)



(b)

Figure 3.11 Luminance distribution of prototype: (a) luminance distribution and crosstalk and (b) normalized luminance distribution

The measured luminance distribution of ten viewpoints in the prototype is plotted as shown in Fig. 3.11. The set of peaks shows the luminance distribution of ten viewpoints at the optimum viewing distance. The normalized luminance distribution as shown in the Fig. 3.11(b) clearly shows that the viewing zone is well duplicated by the dual projection system, and the viewpoints are separated with the uniform gap of 7 mm. The feasibility of the proposed system is verified again through the luminance distribution measurement.

Meanwhile, the luminance value of even-numbered viewpoints (p-polarized) is greater than that of odd-numbered viewpoints (s-polarized). In the previous section, the uniformity issue arises from polarization state of sources. Another factor affecting the uniformity is revealed in the luminance measurement. The difference in projection origin of virtual projectors also raises the uniformity issues. In the Fig. 3.3(b), the projection origin of virtual projectors is separated in the longitudinal direction as well as the lateral direction according to the polarization state of light. Though the longitudinal displacement is less than the lateral displacement, the position of viewpoint generated by virtual projectors would be slightly different in longitudinal direction. Therefore, the captured number of converged rays onto each viewpoint can be altered when the probe of display color analyzer is fixed in the longitudinal direction. The result shows that the viewpoints formed by p-polarized light are close to the probe, and the viewpoints formed by s-polarized are far from the probe. The uniformity issue could be also found in the normalized luminance distribution by comparing the sharpness of peaks. The peak of the p-polarized viewpoints is sharper than that of the s-polarized

viewpoints. In other words, the composite factors of polarization states and projection origin lead to the uniformity issues and high noise ratio of 53% on average. The uniformity can be mitigated by weighting the input images and optimizing the specification of the calcite plate for minimizing the longitudinal shift.

3.4 Summary and discussion

The bandwidth improvement in the multi-projection 3D display is realized by applying the polarization multiplexing in the birefringent crystal. In the birefringent crystal, two possible optical paths exist, and the path can be determined according to the polarization state of light. Dual projection system contributes to forming two different viewing zones at the optimum viewing distance. Therefore, the number of viewing zones in the multi-view system is doubled compared to the conventional system. Furthermore, the full-color image is generated by adopting the temporal multiplexing technique with the real-time polarization switching. The experimental results show that the prototype forms ten viewpoints with five projectors. The luminance distribution at viewing area is measured for analyzing the viewing parameter of view interval and noise. It is confirmed that adjacent viewpoints generated by dual projection are well separated with the interval of 7 mm. The average value of crosstalk is about 53%. Possibilities of improvement in image quality and reduction in noise are discussed: fast-response and diffraction-free polarization switching device, high-resolution projection unit, and accurate alignment of polarization axis. It is expected that the proposed method can be applied in the display system emitting the polarized light such as LC-based display system, laser source based display system, and organic light emitting diodes (OLEDs) having circular polarizer. The capturing system obtaining the 3D information such as light field camera and light field microscopy can be applications of the proposed system. In particular, the concept of the proposed method would be directly implemented in the

light field based multi-projection 3D display system with extended exit pupil beyond the limitation in densely stacking projectors originated by the physical dimension of the device [55].

Chapter 4 Compact multi-focal 3D HMDs with optical path analysis of double refraction

4.1 Introduction

With the popularization of VR technology, the HMD system leads public attentions as the next-generation display. In modern VR HMD system, the immersive and realistic virtual world with large FOV can be constructed by the principle of binocular disparity [13, 14]. In spite of public desire for VR and AR world, there are some issues which should be solved to provide comfort observing circumstances in practical uses. The major issue in the current HMD system is lack of consideration in the human visual system. In practice, mainstream level of HMD device is designed to satisfy the binocular condition of individual who has the interpupillary distance of 65 mm. Besides, most of current systems only present a pair of binocular image in a single depth plane. Thus, many observers are exposed to the visual fatigues originated by accommodation-vergence conflict, pupil swim, and difference in binocular condition of individuals.

Super multi-view and multi-focal systems can mitigate the visual fatigue in conventional VR device by providing multiple perspective images to induce accommodation effect for monocular eye. In the super multi-view

system, two or more view images are projected to monocular eye for inducing the depth cue of accommodation [11, 17, 33, 49, 67, 69]. However, it is hard to implement display optical system providing multiple viewpoints within wearable apparatus, and expand the coverage of super multi-view system inside the eye box where the pupil of human eye moves around. The 3D image reconstruction by multi-focal planes is a good candidate for solving the visual fatigue in the VR system [43, 44, 46, 50-54, 70, 80-85]. There were many works for generating the multi-focal function in 3D display system: physical stacking of display panels [43, 46, 50, 80-84], tunable optical components including liquid lens or deformable mirror [44, 51-54], and polarization-multiplexed multi-focal system using birefringent optical components [70, 85-90].

The simplest way to realize the multi-focal function is to set physical panels in different depth positions. By using the quasi-transparent function of LCDs, two or more LCDs are stacked in the longitudinal direction for implementing the multi-focal function [43, 50, 81]. However, the image quality of the system is severely degraded by the low transparency and the diffraction limit [84]. The state-of-the-art holographic optical element (HOE) technique is proposed for solving the drawbacks in the panel based HMD system [84, 90-96]. The unique functions of both high transparency and resolution free from the diffraction limit are realized by the combination of multiple HOEs and high resolution projection system. Though the HOE is a promising technique for realizing transparency and multi-focal function simultaneously, there are some issues which should be mitigated for commercialization: low efficiency of full-color generation, low uniformity in

reconstructed images, and bulky reconstruction optics.

Tunable optical components including the liquid lens and the deformable mirror are a potential candidate for the multi-focal system. The electrically-controllable shape of tunable optics leads to the modulation of depth position of image [44, 51-54]. By changing the focal length of the liquid lens, the multi-focal function realized via the sequential synchronization of lens shape and display image can show multiple images in different depth positions [44, 52]. Although the adoption of tunable optics improves the degree of freedom in expressible position of images, slow switching speed, noises from intermediate state, optical aberrations from each state, and mechanical issues limit the number of focal planes and system reliability.

Similar to the operation of tunable optics, the sequential change of polarization state also produces the multi-focal function by using birefringent materials such as LC lenses and birefringent optical components [70, 85-89]. By changing eigen polarization state of image, the optical paths in the birefringent material are switched and the multi-focal function appears [97]. By the virtue of fast response of modern polarization rotator, cascade configuration of the birefringent material and the polarization rotator can produce multi-focal function with more than two image planes. However, it is hard to design the system including birefringent materials because of high costs, limitation in selection of materials, manufacturing difficulty, and fragile characteristic [98]. Moreover, the optical aberrations of astigmatism and color dispersion in extraordinary wave increase the complexity of the system [70, 98-100]. Park et al. reported that the astigmatism in the

birefringent crystal blocks the generation of multi-focal function and suppression of axial component by moving slit array was adopted [70]. Those optical aberrations are not fully considered in the previous work and the special aberrations which do not appear in isotropic optical systems should be compensated for commercial uses.

In this chapter, the compact 3D HMD system with multi-focal function is implemented. The multi-focal function is realized by the double refraction in the Savart plate, a crossed pair of birefringent plates having the same specifications. The manufacturing process and the design of the optical system considering aberrations in the plane-parallel birefringent plate having two faces plane and parallel are easier than that of birefringent lenses and mirrors. For retaining the robustness of multi-focal function, the astigmatism and the color dispersion in the Savart plate are investigated. Both the astigmatism and the chromatic aberration are compensated by modification of the Savart plate with symmetric optical configuration and sub-pixel switching method, respectively. The micro OLED with high pixel density of 1666 pixels per inch is duplicated in the longitudinal direction according to the polarization state. The multi-focal planes of micro OLED are combined with the beam splitter and the concave mirror for realizing the AR function. From well-defined geometrical relation of the separated image planes, layer images of compressive light field display are calculated for reconstructing the dense viewpoints inside the eye box of the HMD [43, 83]. In the experiments, the prototype for monocular eye and the real-time operation with synchronization between the display image and the polarization rotator are implemented. The results verify that both the astigmatism and the

chromatic aberration of extraordinary wave are mitigated. The perspective images are observed with the change of observing position inside the eye box. The implemented prototype also convinces the high quality 3D images and satisfaction of wearable function with a small form factor.

4.2 Principle of multi-focal 3D HMD system

4.2.1 Multi-focal 3D HMD system using Savart plate

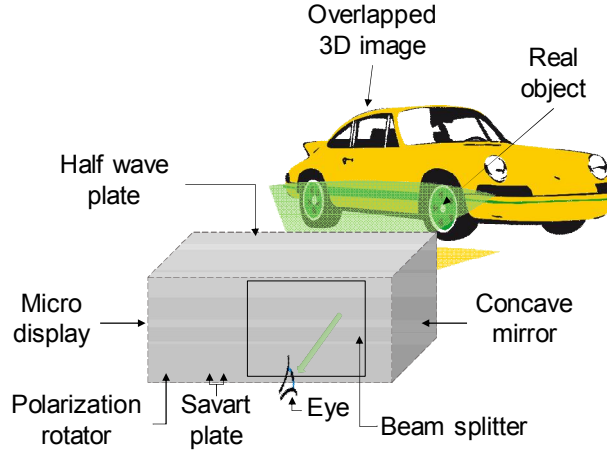


Figure 4.1 Schematic diagram of multi-focal 3D HMD system using Savart plate

The basic concept of the proposed system is the optical duplication of the micro display in the longitudinal direction. The optical duplication of the micro display is realized by the polarization-multiplexed optical path switching method in the birefringent crystal. The Savart plate which is comprised of a pair of plane-parallel birefringent plate can be applied to duplicate the micro display in longitudinal direction [101]. To mitigate the astigmatism of extraordinary wave, half wave plate (HWP) is inserted in the middle of the Savart plate as shown in Fig. 4.1. The detailed analysis of astigmatism compensation is performed in the following section. The polarization state of the micro display is modulated by the fast switching

polarization rotator. By altering the eigen polarization state of image in sequence, two virtual image planes are formed in different longitudinal positions. From the optically duplicated image planes, the 3D images can be realized by adopting the principle of depth-fused (DFD) display or compressive light field display. While the resolution of the multi-focal system based on LCD panels is limited by the diffraction of periodic pixelated structure, the optical duplication of the display panel is free from the diffraction limit. Therefore, it is possible to present the high resolution images by adopting the high resolution micro display. Besides, since two virtual panels share the inherent device characteristic of display, color reproductivity and uniformity issues can be easily considered.

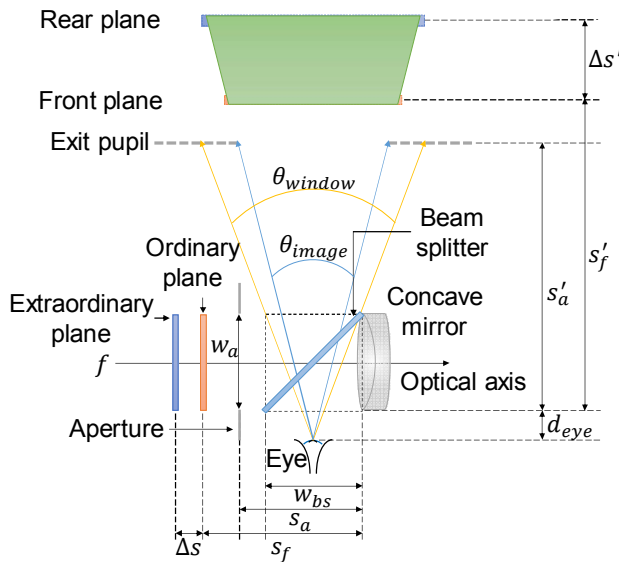


Figure 4.2 Optically equivalent model of multi-focal HMD system using Savart plate

Figure 4.2 shows the optical equivalent model of the proposed system. The duplicated planes can be floated by concave mirror or convex lens for separating those planes in the longitudinal direction and the AR function is also realized by combining the beam splitter. The simple configuration of optical components contributes to retaining the small form factor, so that it satisfies the wearable function. From the equivalent model, the FOV, and the positions of virtual planes are calculated through the geometric relation between each of optical components.

$$\theta_{window} = 2 \tan^{-1} \left(\frac{W_{bs}}{2(d_{eye} + W_{bs})} \right), \quad (4.1)$$

$$\theta_{image} = 2 \tan^{-1} \left(\frac{W_a}{2(d_{eye} + S_a)} \right), \quad (4.2)$$

where θ_{window} and θ_{image} are the FOVs of the real world scene and the display image, respectively. W_{bs} is the width of beam splitter aperture and d_{eye} is the distance between eye pupil and entrance of the HMD module. When the eye pupil is located at the entrance of the module, the θ_{window} is maximized with the value of 53 °. The FOV of the display image is calculated by the width of aperture in the display part W_a and the distance between the aperture and the concave mirror S_a . In the display part, the aperture is determined by relative size difference between active area of the micro display and the Savart plate.

When duplicated planes are separated by Δs , and both planes are located

inside the focal length f of concave mirror or convex mirror, the separation distance Δs is magnified as follows:

$$\Delta s' = \frac{\Delta s}{(s_f - f)(s_f + \Delta s - f)} f^2, \quad (4.3)$$

where s_f is the position of duplicated panel near the concave mirror. From Eq. (4.3), the geometrical relation of multi-focal function is defined and the 3D images can be reconstructed between both panels. The displacement Δs between duplicated planes is dependent on many parameters: the thickness of the Savart plate, the birefringence of material, the orientation of optic axis, and the wavelength of light. For clarifying the relation between system parameters and the optical characteristic of the Savart plate such as image displacement and aberrations, ray tracing simulation considering those parameters is performed in following sections.

4.2.2 Astigmatism compensation by modified Savart plate

In order to investigate the polarization-dependent multi-focal function and the astigmatism in the Savart plate, the light ray cone passing through the Savart plate is analyzed with the variables of optic axis orientation. The commercialized calcite plate with the optic axis with 45° to incident plane is used for simulation and implementation of the prototype.

Table 4.1 Simulation conditions for astigmatism analysis in birefringent plate

Specifications	Values
Size of single calcite plate	30 mm (W) \times 30 mm (H) \times 15 mm (D)
Range of diverging angle	From -5° to 5°
Orientation of optic axis	45° to incident plane

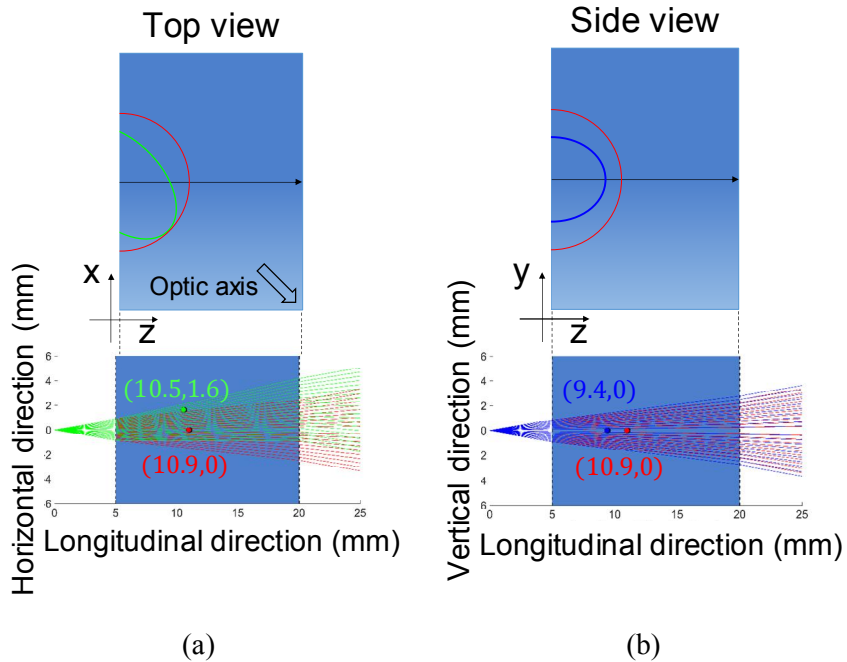


Figure 4.3 Astigmatism in plane-parallel calcite plate: ray tracing for (a) horizontal component (top view) and (b) vertical component (side view)

In the birefringent crystal, the optical aberration of the astigmatism appears, since the refractive index for extraordinary wave changes according to the plane of incidence. As shown in Figs. 4.3(a) and 4.3(b), the normal surface shells of index ellipsoid for horizontal and vertical components of extraordinary wave differ when the light ray cone is incident on the plane-

parallel calcite plate which has the thickness of 15 mm and the optic axis with 45° to the incident plane. The detailed simulation conditions are shown in Table 4.1. For both cases, the ray tracing is performed and the virtual image of point light source is evaluated. The horizontal component in Fig. 4.3(a) shows both longitudinal and lateral shifts of the point light source, but the vertical component in Fig. 4.3(b) only shows the longitudinal shift. Since both components form two different virtual point light sources, the astigmatism appears when the image is observed through the plate. Thus, the anamorphic characteristic of single birefringent crystal is not proper to implement the multi-focal function.

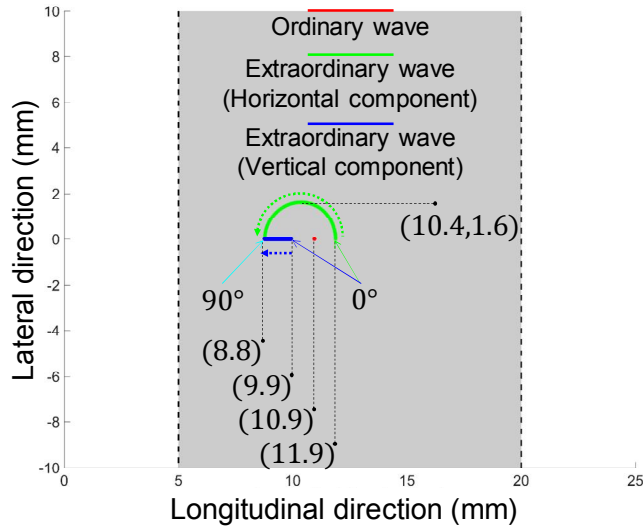


Figure 4.4 Trajectory of virtual image of point light source with angle of optic axis

In Fig. 4.4, locus of virtual images of the point light source is investigated with the changes of optic axis orientation. When the optic axis is

placed on the incident surface, the virtual images of the horizontal and the vertical components of extraordinary wave are formed at positive and the negative side from that of ordinary wave, respectively. As the angle of optic axis to the incident surface increases, the point light source of the horizontal component is shifted in the counterclockwise direction and that of the vertical component is shifted in the negative-longitudinal direction. Near the optic axis with 90° , the point light sources of both components are almost coincidence, but it is hard to utilize the linear polarization state as the eigen polarization state. Both azimuth and radial polarization are the eigen polarization of plane-parallel birefringent plate with the optic axis perpendicular to incident surface [100]. Thus, the single birefringent crystal is not appropriate to generate the multi-focal function [70].

In the isotropic optical system, the astigmatism is compensated by the anamorphic lenses. However, in the proposed system, the calcite plate only acts as the anamorphic lens for extraordinary wave. The isotropic anamorphic lens can mitigate the astigmatism of extraordinary wave, but the astigmatism of ordinary wave would arise. For solving the astigmatism in birefringent crystal, the Savart plate can be used to cancel out the anamorphic function. In normal Savart plate, the eigen polarization state acts as both ordinary and extraordinary waves at the 1st and the 2nd plate, respectively. Therefore, the astigmatism from extraordinary wave still remains. The modified structure of the Savart plate in which the HWP is inserted between plates can solve the astigmatism [100]. If the Savart plate is modified, each axial component of extraordinary wave would experience two different shapes of normal surface shell and the optical compensation of

astigmatism.

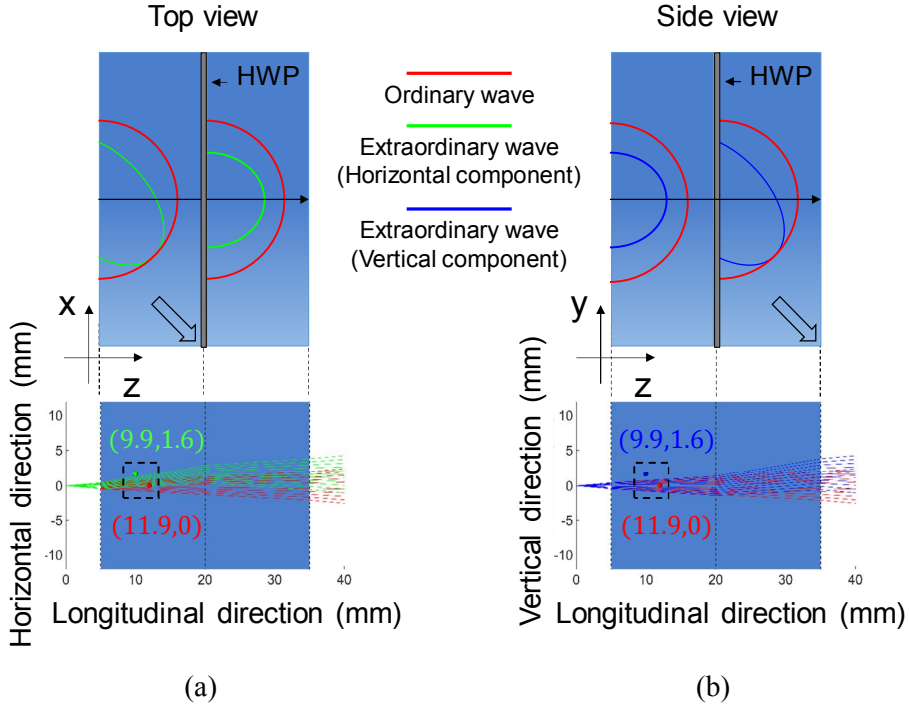


Figure 4.5 Astigmatism compensation using Savart plate with half wave plate: (a) horizontal component (top view) and (b) vertical component (side view)

Figure 4.5 shows the ray tracing results in modified Savart plate. In the 1st calcite plate of the Fig. 4.5(a), the horizontal component of extraordinary wave experiences the intersection of normal surface shell for which the major axis of ellipse is rotated by 45° to the incident surface. After passing through the 1st plate, the polarization state of ray is rotated by 90° by the HWP. The eigen polarization is switched and the extraordinary wave passing

through the 1st plate still acts as extraordinary wave in the 2nd plate, but the shape of normal surface shell is changed to that for vertical component in the 1st plate as shown in Fig. 4.5(b). In the 2nd plate, the horizontal component of extraordinary wave experiences the intersection of normal surface shell of which the major axis of ellipse is placed along the longitudinal direction. Therefore, the ray trajectory of horizontal component is affected by both shapes of normal surface shells. Likewise, the vertical component of extraordinary wave is also affected by two different shapes of normal surface shells as shown in Fig. 4.5(b). The optical paths in the HWP are ignored because the thickness of the HWP is so small. The tracked rays from the point light source show that positions of the virtual image calculated by each component are one-to-one coincidence in both lateral and longitudinal directions. The results present that the astigmatism of single birefringent crystal is cancelled by the modified Savart plate and the exact position of virtual images is defined. Thus, the multi-focal function is realized by the simple structure of the modified Savart plate and it is possible to duplicate the array of pixels in the micro display. Under the simulation condition in the Table 4.1, the longitudinal displacement between both virtual images of ordinary and extraordinary wave is about 2 mm. The lateral displacement is about 1.6 mm. The image dislocation of two panels by lateral displacement can be mitigated by pixel shifting or dual layer of modified Savart plate [100]. Since the displacement is directly proportional to the thickness of the crystal, the magnitude of displacement per thickness can be calculated and the values in the longitudinal and the lateral directions are 0.0674 and 0.0549 mm per unit thickness of the Savart plate, respectively.

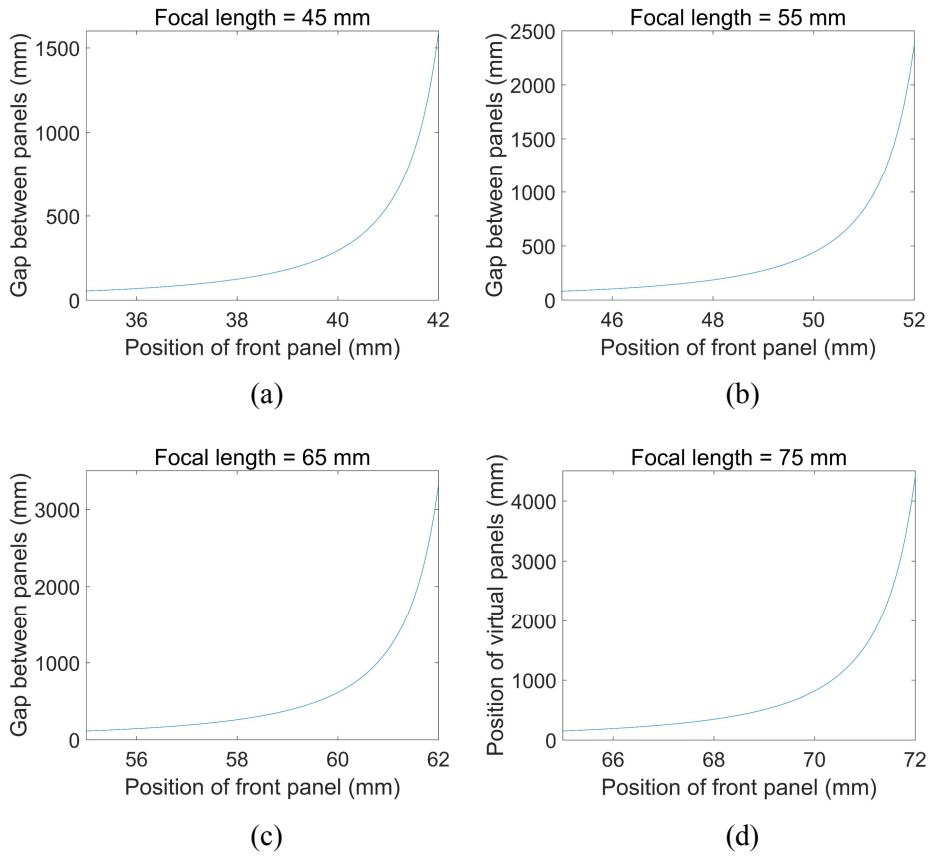


Figure 4.6 Relationship between focal length of mirror and position of virtual planes: (a) focal length = 45 mm, (b) focal length = 55 mm, (c) focal length = 65 mm, and (d) focal length = 75 mm

The gap between virtual panels is determined by the focal length of mirror as well as the gap between duplicated panels. When the longitudinal displacement is fixed as 2 mm, the gap between virtual panels is calculated with the focal length of mirror shown in Fig 4.6. With the increase of the focal length, the gap between virtual panels is also increased. In consequence, the gap between front and rear panel can be optimized by modifying the

system parameters such as the thickness of the modified Savart plate, the focal length of mirror, and the position of micro display.

4.2.3 Analysis on lateral chromatic aberration of extraordinary plane

The color dispersion in the imaging system is an important issue which should be considered to present clear images. Though the wavelength is a major factor of the color dispersion in the isotropic optical system, the color dispersion in the birefringent material is affected by the polarization state of image as well as wavelength because the refractive index is dependent on both the wavelength and the polarization state. For analyzing the color dispersion, the spectrum of micro OLED with high pixel density (Olightek, SVGA050, China) is measured by the spectrometer (Ocean optics, USB4000-VIS-N, USA) as shown in Fig. 4.7. The center wavelengths of three-primary sub-pixels of micro OLED are evaluated by calculating power-weighted mean wavelength as follows:

$$\lambda_c = \frac{1}{P_{total}} \int p(\lambda) \lambda d\lambda, \quad (4.4)$$

where λ_c is the center wavelength of primary sub-pixels, P_{total} is the total power of the spectral density, p is the power spectral density of micro OLED, and λ is the wavelength of emitted light. The spectral components more than 50 percent of intensity counts are considered in center wavelength

calculation, and minor components of side lobe are neglected in calculation.

Table 4.2 Simulation conditions for color dispersion analysis in modified Savart plate

Specifications	Values
Size of single calcite plate	30 mm (W) \times 30 mm (H) \times 15 mm (D)
Range of diverging angle	From -5° to 5°
Orientation of optic axis	45° to incident plane
Range of wavelength	From 400 nm to 700 nm
Center wavelength	Red: 609 nm, Green: 509 nm, Blue: 488 nm
Pixel pitch of micro OLED	15 μ m

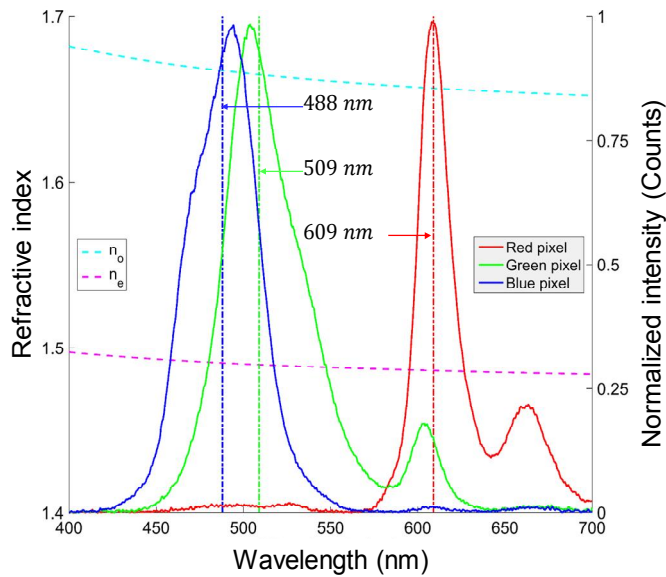


Figure 4.7 Spectrum of micro OLED and center wavelength, (b) chromatic aberration in modified Savart plate

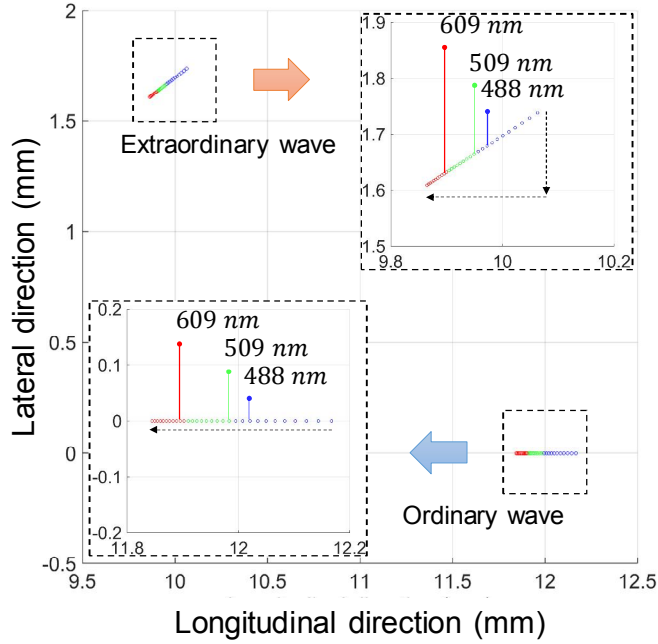


Figure 4.8 Chromatic aberration in modified Savart plate

For each eigen polarization state, the refractive index of calcite crystal is defined by Sellmeier equation as follows [102]:

$$\begin{cases} n_o = 2.69705 + 0.0192064 / (\lambda^2 - 0.01820) - 0.0151624\lambda^2, \\ n_e = 2.18438 + 0.0087309 / (\lambda^2 - 0.01018) - 0.0024411\lambda^2, \end{cases} \quad (4.5)$$

where n_o is the refractive index for ordinary wave and n_e is the refractive index of extraordinary wave. After the calculation of refractive index for each polarization state and wavelength, the ray tracing is performed. Figure 4.8 shows the color dispersion relation in both ordinary and extraordinary

waves. For ordinary wave, only longitudinal chromatic shift occurs likewise the situation that the white light source passes through the isotropic glasses. On the contrary, for extraordinary wave, both longitudinal and lateral chromatic shifts occur. Though it is hard to observe the affection of longitudinal chromatic shift through the imaging system with large depth of focus (DOF) such as the human visual system, the lateral chromatic shift highly degrades the image quality. In particular, the human visual system is more sensitive in recognizing the chromatic aberration in the lateral direction. As shown in Fig. 4.8, the chromatic shift in the lateral direction occurs within the range of 500 μm . Since it is known that the human eye distinguishes the spatial difference of image with an angle of one minute of arc, the lateral chromatic shift of the panels generated by extraordinary wave can be observed when the image is magnified by concave mirror or convex lens. In addition, the disregard of chromatic shift would distort the realization of 3D image from DFD or compressive light field display which reconstructs the 3D image by pixel mapping among multiple panels. In the isotropic optical system, the chromatic aberration is compensated by combination of multiple lenses and groups with different materials. However, it is hard to compensate the chromatic aberration in the birefringent optical component with same methodology of the isotropic system because of high costs and difficulty in selection of birefringent materials. The combination of two different birefringent materials could reduce the chromatic aberration, but the astigmatism will occur because of difference between the refractive indexes of materials [98]. In this case, the image processing of primary source channel shift in opposite direction of chromatic aberrations could be

better and simple way to compensate the lateral chromatic shift. The degree of shift is approximated by converting the displacement of chromatic shift to the number of sub-pixels as follows:

$$\begin{cases} N_{green} = \left[\frac{\Delta C_{green} - p_{sub}}{p_p} \right], \\ N_{blue} = \left[\frac{\Delta C_{blue} - 2p_{sub}}{p_p} \right], \end{cases} \quad (4.6)$$

where N_{green} and N_{blue} are the number of shifts for green and blue sub-pixels, respectively. ΔC_{green} and ΔC_{blue} are the lateral chromatic shift of green and blue colors. The notation $[\cdot]$ presents the function of rounding off to the nearest integer. Since the micro OLED has the red, green, and blue stripe sub-pixel structure and the reference of the chromatic shift is red-colored sub-pixel, the horizontal pixel shift should be calculated by considering sub-pixel pitch of p_{sub} . On the other hand, the vertical pixel shift is approximated by the pixel pitch of p_p , and the p_{sub} in the Eq. (4.6) is vanished. Under the simulation condition in Table 4.2, the green color shift values in horizontal and vertical direction are 3 and 2 pixels, respectively. For blue color, the 4 and 3 pixels shifting in horizontal and vertical directions is required for chromatic aberration compensation.

4.2.4 Additive type compressive light field display

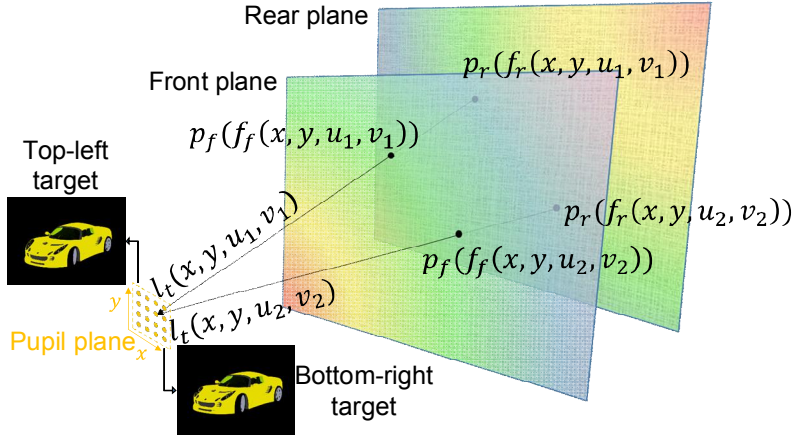


Figure 4.9 3D image reconstruction by light field optimization for two additive layers and (b) real-time operation of two additive layers

The multi-focal function can reconstruct the 3D images using the principle of DFD or compressive light field display. Since the DFD provides only a single viewpoint at the fixed pupil position, usually eye- or gaze-tracking techniques should be accompanied to provide correct view images with the pupil swim [103]. In case of the compressive light field display system, it is possible to generate multiple viewpoints with corresponding perspective images near the eye pupil [43, 83, 104]. Though the correlation among the view images in the compressive light field display system is lower than that in the DFD system with eye-tracking, a moderate correlation for reconstructing high quality 3D image can be provided when the optimized area is limited inside the eye box. Thus, the compressive light field display can be a good candidate for the 3D HMD system without the tracking

techniques. Since both panels are transparent and independent to each other in the proposed method, the observed image can be presented by the summation of images from each panel as shown in Fig. 4.9. For generating the layer images, the additive type compressive light field display method is adopted as follows [81, 84]:

$$l_t(x, y, u, v) = p_f(f_f(x, y, u, v)) + p_r(f_r(x, y, u, v)), \quad (4.7)$$

where l_t is the target light field of the 3D image for a single viewpoint, and p_f and p_r are pixel information of front and rear layers, respectively. f_f and f_r are mapping functions of front and rear planes. x and y are the positions of pixels corresponding to the target light field. u and v are the tangential components of the target light field. For the entire viewpoints and their corresponding perspective images inside the eye box, layer images for panels are optimized by solving the least square algorithm [83].

Figure 4.10 shows the real-time synchronization of each optical component. During the switching of duplicated panels to present correct layer images, the LC response in the polarization rotator is controlled by applied voltage to modulate the oscillation axis of linear polarization. After synchronization, the correct layer images are presented on each image plane and the 3D images with correct perspective views are observed inside the eye box.

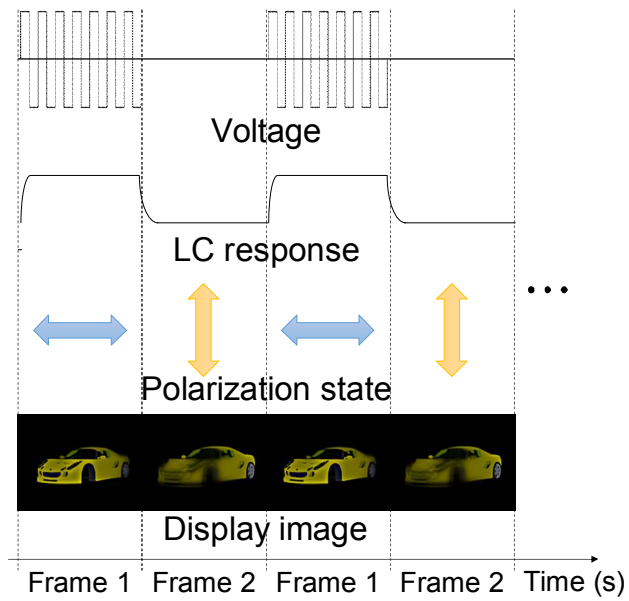


Figure 4.10 Real-time operation of two additive layers

4.3 Implementation of prototype of multi-focal 3D HMD system

For investigating the feasibility of the proposed system and the reliability in simulation results about optical aberrations, the prototype of the multi-focal 3D HMD system for monocular is implemented.

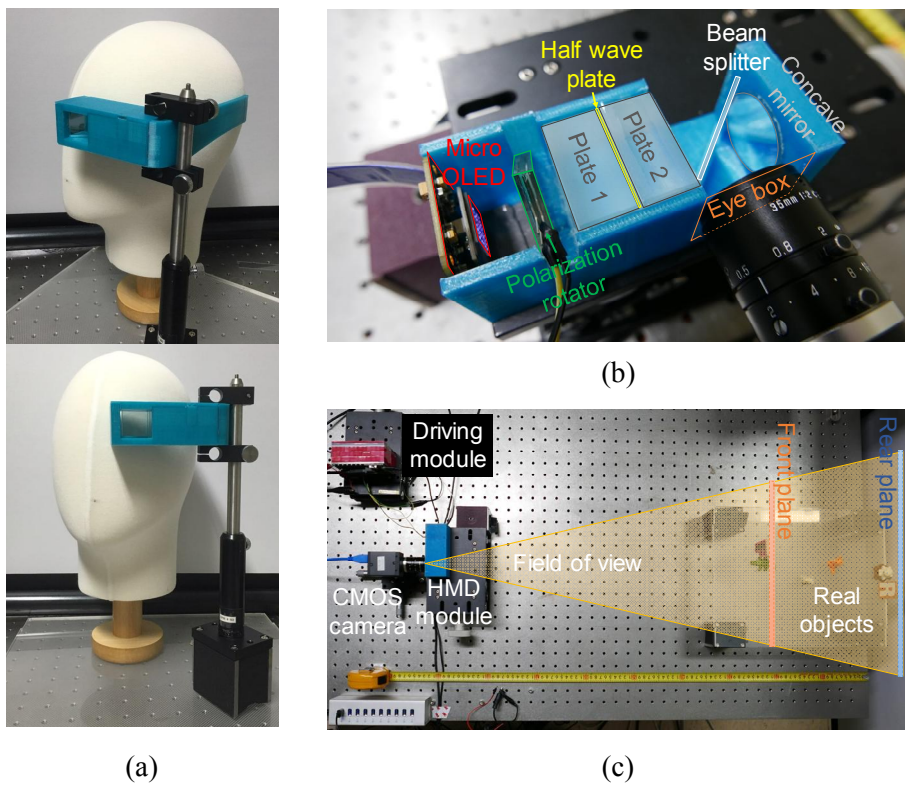


Figure 4.11 Experimental setup: (a) wearable function of proposed system, (b) detailed configuration of HMD module, and (c) experimental setup with real objects

Simple optical structure in the HMD module provides wearable function as shown in Fig. 4.11(a). The mannequin having the size of 200 mm (W) by 200 mm (H) by 230 mm (D) can wear the HMD module of the proposed system. The HMD module is operated by connecting to power and video cables from personal computer. The personal computer can be simply replaced by portable devices or integrated circuit. In Fig. 4.11(b), the detailed configuration of the module is introduced. The polarization state of the micro OLED with high pixel density is modulated by the polarization rotator (LC-Tec, PolarSpeed[®]-M(L), Sweden) in real-time. After passing through the modified Savart plate, two virtual display panels are formed according to the eigen polarization state. The separation distance of two panels is expanded by the concave mirror and the beam splitter deflects the orientation of images. In the prototype, the concave mirror is employed to exclude the affection from the chromatic aberration in the convex lens. Complementary metal-oxide-semiconductor (CMOS) camera is located at the entrance of the module and captures the perspective images inside the eye box. The operation voltage of the polarization rotator and display images for both planes are synchronized at 30 Hz. As shown in Fig. 4. 11(c), two virtual planes are floated in the space with separation distance of 260 mm. Both real objects and 3D images are observed simultaneously. The FOV of 3D image in the prototype is limited by the small size of the micro OLED, and the values are 8.9 ° and 6.3 ° in horizontal and vertical direction, respectively. The FOV of 3D image can be improved by applying large-sized display and concave mirror or convex lens with short focal length. The maximum FOV of 3D image of 37 ° is evaluated when the size of micro display is equal to

that of the Savart plate and the active area of the display sticks to the entrance of the Savart plate. The detailed experimental conditions are presented in Table 4.3.

Table 4.3 Experimental conditions for compact multi-focal 3D HMD display system using Savart plate

Specifications	Values
Size of HMD module	90 mm (W) by 40 mm (H) by 40 mm(D)
Weight of HDM module	131 g
Size of calcite plate	30 mm (W) \times 30 mm (H) \times 15 mm (D)
Active area of micro OLED	12 mm (W) \times 9 mm (H)
Resolution of micro OLED	800 \times 600
Refresh rate of micro OLED	60 Hz
Polarization contrast	20:1
Refresh rates of polarization rotator	540 Hz
Focal length of concave mirror	75 mm
Distance of ordinary plane	640 mm
Distance of extraordinary plane	900 mm
Field of view for real world scene	53 °
Maximum field of view	37 °
Field of view in prototype	8.9 ° in horizontal direction 6.3 ° in vertical direction



(a)



(b)

Figure 4.12 Focus changes between virtual planes: (a) focus change without compensation and (b) focus change with compensation

Figure 4.12 shows the verifications of the multi-focal function and the chromatic aberration compensation results. When the CMOS camera with

small DOF lens captures the image at the positions of 640 mm, 770 mm and 900 mm, the shape of image changes. When the camera focuses on the front plane 640 mm away from the eye box, the real object of 'F' and computer-generated image of 'Front' are clearly observed without blur. On the contrary, other real objects of 'C' and 'R' and the image of 'Rear' are blurred. When the camera focuses on the real object of 'C' located in the middle of both front and rear planes, both virtual images are blurred. Camera focusing on rear plane captures clear image of 'Rear' and the object of 'R'. The results of focus change verify that the multi-focal planes are well defined without the astigmatism. When the original image without compensation is inserted as the input, the magnified image in Fig. 4.12(a) shows the chromatic shift in lateral direction as expected in the simulation results of Section 4.2.3. Assuming that the red color is reference of the color shift, the blue color is shifted to the bottom-right direction. The lateral chromatic shift of each color is calculated and the base image is processed to apply the sub-pixel shifting method. When the compensated image that blue and green channels are shifted to the top-left direction is applied to the rear plane of extraordinary wave, the chromatic shift is reduced and clear white image is observed as shown in Fig. 4.12(b). The result verifies the feasibility of analysis on the lateral chromatic aberration and the sub-pixel shifting method.

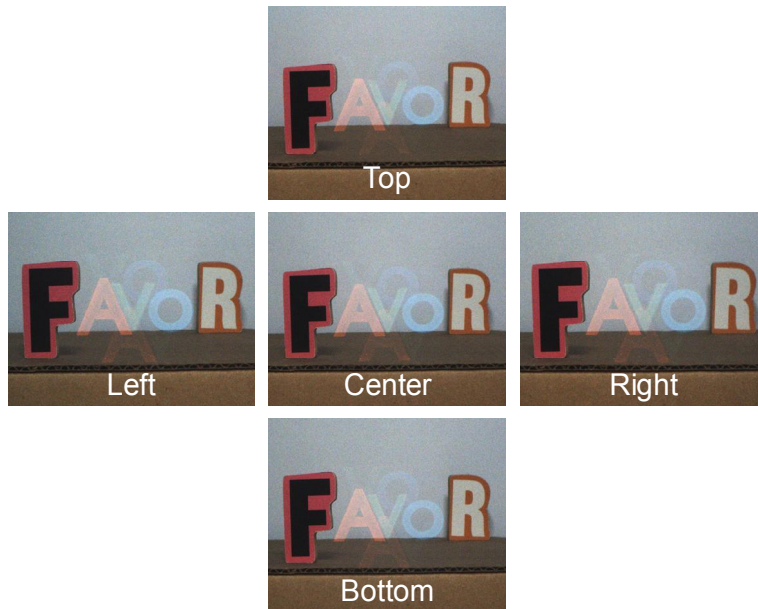


Figure 4.13 Perspective images in compact 3D HMD system

Figure 4.13 presents the perspective changes of 3D image generated by the compressive light field display inside the eye box. The base images for both planes are optimized at viewpoints inside the eye box with 2 mm interval. The size of the eye box is 24 mm by 24 mm with 169 viewpoints. For investigating the perspective of 3D images containing three characters, series of perspective images are captured at the edge of the eye box. As shown in Fig. 4.13, three characters of 'A', 'V', and 'O' are computer-generated 3D images and real objects of 'F' and 'R' are arranged to make the word 'FAVOR'. The character 'A' and 'O' are located at the same depth position of the object 'F' and 'R', respectively. The character 'V' is located in the middle of real objects. The relative perspective changes between real objects and computer generated images verify the correct reconstruction of

3D image in the space. The results show that both the object 'F' and image 'A' are located at the front plane and the object 'R' and 'O' are located at the rear plane. Though the eye box is so small with the size of 24 mm by 24 mm, which means that the perspective of 3D image is also small, clear and appropriate perspectives are observed. In captured images, ghost images are observed on both upper and lower sides. It is induced from low polarization contrast of polarization rotator and mismatch between scanning of micro display and switching of rotator. Unintended portion of the eigen polarization component acts as the leakage of ghost image. The polarization rotator with high polarization contrast and black offset image between each state can mitigate the crosstalk from ghost image as stated in Chapter 3.

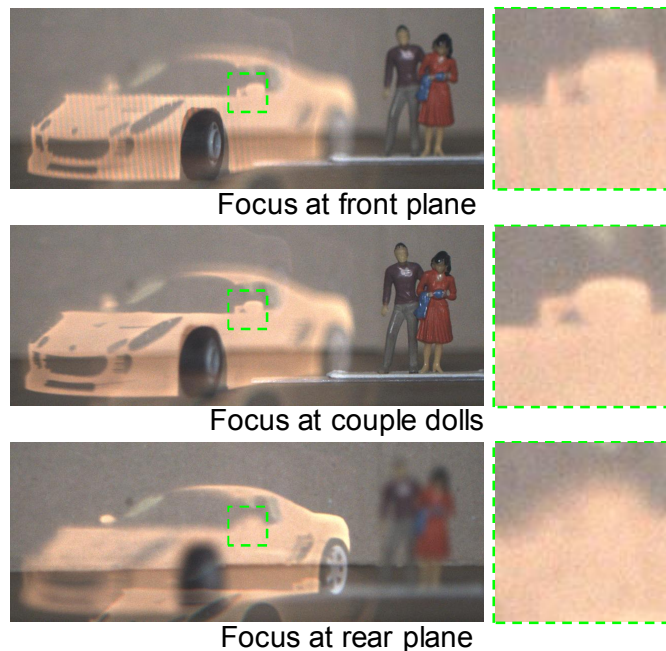


Figure 4.14 Focus changes in compact 3D HMD system

In Fig. 4.14, the focus change of car which is configured along front plane to rear plane is also provided. The front tire and couple dolls are real objects, and the car body and rear tire are computer-generated 3D images. The couple dolls are located at the depth position of rear-view mirror. As shown in Fig. 4.14, the focus change is confirmed by comparing the degree of blur in the magnified images of the rear-view mirror. The integration of real object and its information can be applied for diverse purposes in industrial, medical, and educational fields. In addition, the compressive light field images generated by the multi-focal planes can contribute to relieving the visual fatigue [43, 83]. From the experimental results, the feasibility of the multi-focal function with the aberration compensation and the realization of 3D images in the prototype are confirmed.

4.4 Summary and discussion

Realization of 3D HMD with multi-focal function is proposed by using the modified Savart plate. The HWP is inserted in the middle of Savart plate composed of plane-parallel calcite plates to compensate the astigmatism. High resolution micro OLED with 1666 ppi is optically duplicated into two virtual panels in longitudinal direction. To assure the high quality 3D image in the proposed system, the color dispersion of extraordinary wave is also examined. By applying the sub-pixel shifting method for three primary color channels, the lateral chromatic aberration of extraordinary wave is effectively reduced. The AR function with 3D images is realized by combining the duplicated panels with the concave mirror and the beam splitter. From the geometrical relation between two panels, the compressive light field images are represented by optimizing the light field of additive layers. Through the experiments, the prototype of the proposed system is implemented. As the polarization rotator and the display image are synchronized in real-time with 30 Hz, the multi-focal function and the aberration compensation are confirmed. The perspective of 3D image is also verified by comparing to the real objects. Simple optical structure realizes the wearable function of the HMD module in spite of the combination of the beam splitter. The size of the module is about 40 mm (W) by 90 mm (H) by 40 mm (D) and the weight is 131 g. The form factor of the system can be minimized by optimizing the specification of optical components such as focal length of mirror and the size of display. Besides, the FOV of the system can be improved by adopting large-sized micro display and reducing distance

between the display and the concave mirror. The image distortion from pupil swim can be minimized by pre-distortion rendering of target perspective images [64]. The proposed system can contribute to implementation of the 3D HMD with multi-focal function over two or more focal planes by combining the multiple sets of the modified Savart plate, tunable lenses or deformable mirrors. Moreover, the simple optical configuration and optical aberration compensation in the proposed system will realize the high quality 3D image in the wearable display system such as the HMD and the smart watch.

Chapter 5 Conclusion

With a longing for freshness in visual experience, the VR and AR systems provoke boom in the display industry and the market. The reconstruction of 3D image is essential component for both systems. Though there has been commercialized 3D display technology integrated in the 3D TV and the theater, low level of 3D resolution and visual discomforts from lack of consideration in human perception lead to failure in the market. For satisfying the desire of the public familiar to high level of 2D display devices, high quality 3D images and viewing characteristics should be guaranteed.

Realization of high bandwidth by multiplexing technique or restricting of viewing parameters such as the viewing region and the number of viewers is required in order to provide high level of 3D images with the current display technology. The multi-projection 3D display system for public 3D display and the HMD system for individual are introduced for potential candidates satisfying those requirements. However, the complex system configuration in the multi-projection 3D display and lack of depth cue in the HMD should be compensated for practical uses.

In this dissertation, two optical phenomena of the TIR and the double refraction are investigated to implement compact 3D display systems providing high quality 3D images: the TIR in the optical light-guide realizes the compact multi-projection 3D display system, and the double refraction in the birefringent crystal improves the bandwidth of both the multi-projection 3D display system and the HMD system. Those materials are optically

transparent, but the optical path in the material is governed by unique optical phenomena according to the status of the light. By tracing the optical path in the material, methods for realizing the compact systems is proposed and the image characteristics in the proposed systems are investigated. Through the implementation of each prototype, the feasibility of the systems is examined.

In the multi-projection 3D display, the sufficient projection distance is required for presenting large-sized image. By adopting the optical light-guide, the projection distance in the horizontal direction is effectively reduced. The image information incident on the optical light-guide is successfully folded in multiple times by the TIR and the horizontal projection distance is converted to the vertical direction. For simplifying the analysis of view image distortion, the equivalent model of the optical light-guide is deduced and the distortion in each view image is compensated by pre-distortion method. In the experiment, the ten-view multi-projection 3D display system with reduced projection space is implemented. The projection distance of the system is reduced as 18% of the conventional multi-projection 3D display system.

The double refraction in the birefringent crystal is adopted in both the multi-projection 3D display and the HMD systems for improving the bandwidth. Since the optical path in the birefringent material is different with the polarization state of the light and the orientation of optic axis, it is possible to apply the polarization multiplexing technique with simple optical configuration.

In the multi-projection 3D display system, the birefringent crystal is designed to duplicated the viewing zone in the lateral direction. Thus, the

single projection unit expresses two adjacent viewing zones. Through the experiments, the prototype including the birefringent plate, the polarization rotator, and five projectors is implemented. The polarization rotator and each projector are synchronized for polarization multiplexing and ten viewing zones are formed at the optimum viewing zone.

In the HMD system, the multi-focal function is realized by adopting the longitudinal shift of image plane in the birefringent crystal. The astigmatism and the color dispersion in the birefringent plate are investigated by the ray tracing simulation. Modified Savart plate composed of a pair of crossed birefringent plates optically compensates the astigmatism and sub-pixel shifting of original image computationally compensates the lateral chromatic aberration. From the compensation of aberrations, the well-defined multiple image planes are formed in the prototype and the 3D image is reconstructed by the compressive light field display. The compact multi-focal 3D HMD module has the size of about 40 mm (W) by 90 mm (H) by 40 mm (D) and the weight of 131 g. In the experiments, the multi-focal function and the 3D image reconstruction are verified by the camera focus change and the perspective investigation, respectively.

Bibliography

1. B. Lee, “Three-dimensional displays, past and present,” *Phys. Today* **66**(4), 36-41 (2013).
2. J. Geng, “Three-dimensional display technologies,” *Adv. Opt. Photonics* **5**(4), 456–535 (2013).
3. N. S. Holliman, N. A. Dodgson, G. E. Favalora, and L. Pockett, “Three-dimensional displays: a review and applications analysis,” *IEEE Trans. Broadcast* **57**(2), 362-371 (2011).
4. H. Urey, K. V. Chellappan, E. Erden, and P. Surman, “State of the art in stereoscopic and autostereoscopic displays,” *Proc. IEEE* **99**(4), 540–555 (2011).
5. B. Javidi and F. Okano, eds., *Three-dimensional television, video, and display technologies*, (Springer, New York, 2002).
6. T. Okoshi, “Three-dimensional displays,” *Proc. IEEE* **68**(5), 548–564 (1980).
7. A. Stern and B. Javidi, “Three-dimensional sensing, visualization and processing using integral imaging,” *Proc. IEEE* **94**(3), 591–607 (2006).
8. J. Hong, Y. Kim, H.-J. Choi, J. Hahn, J.-H. Park, H. Kim, S.-W. Min, N.Chen, and B. Lee, “Three-dimensional display technologies of recent interest: principles, status, and issues [Invited],” *Appl. Opt.* **50**(34), H87–H115 (2011).
9. D. M. Hoffman, A. R. Girshick, K. Akeley, and M. S. Banks, “Vergence-accommodation conflicts hinder visual performance and cause visual fatigue,” *J. Vis.* **8**(3), 33 (2008).

10. Y. Kim, J. Kim, K. Hong, H. K. Yang, J.-H. Jung, H. Choi, S.-W. Min, J.-M. Seo, J.-M. Hwang, and B. Lee “Accommodative response of integral imaging in near distance,” *J. Disp. Technol.* **8**(2), 70–78 (2012).
11. J. Nakamura, K. Tanaka, and Y. Takaki, “Increase in depth of field of eyes using reduced-view super multi-view displays,” *Appl. Phys. Express* **6**(2), 022501 (2013).
12. E. B. Goldstein, *Sensation and Perception*, 9th ed. (Cengage Learning, 2014)
13. C. Wheatstone, “On some remarkable, and hitherto unobserved, phenomena of binocular vision,” *Philos. Trans. R. Soc. London* **128**, 371–394 (1838).
14. E. A. Edirisinghe and J. Jiang, “Stereo imaging, an emerging technology,” in *Proceedings of SSGRR*, (L’Aquila, Italy, 2000) 6.
15. F. E. Ives, “A novel stereogram,” *J. Franklin Inst.* **153**(1), 51–52 (1902).
16. T. Honda, Y. Kajiki, S. Susami, T. Hamaguchi, T. Endo, T. Hatada, and T. Fujii, “A display system for natural viewing of 3-D images,” in *Three-dimensional television, video and display technologies*, B. Javidi, F. Okano ed. (Springer-Verlag, Berlin Heidelberg, Germany, 2002) 461–487.
17. Y. Takaki, Y. Urano, S. Kashiwada, H. Ando, and K. Nakamura, “Super multi-view windshield display for long-distance image information presentation,” *Opt. Express* **19**(2), 704–716 (2011).
18. D. Fattal, Z. Peng, T. Tran, S. Vo, M. Fiorentino, J. Brug, and R. G. Beausoleil, “A multi-directional backlight for a wide-angle glasses-free three-dimensional display,” *Nature* **495**, 348–351 (2013).

19. J. Kim, C.-K. Lee, Y. Jeong, C. Jang, J.-Y. Hong, W. Lee, Y.-C. Shin, J.-H. Yoon, and B. Lee, "Crosstalk-reduced dual-mode mobile 3D display," *J. Disp. Technol.* **11**(1), 97–103 (2015).
20. G. Lippmann, "Epreuves reversibles donnant la sensation du relief," *J. Phys.* **7**, 821–825 (1908).
21. F. Okano, H. Hoshino, J. Arai, and I. Yuyama, "Real-time pickup method for a three-dimensional image based on integral photography," *Appl. Opt.* **36**(7), 1598–1603 (1997).
22. B. Lee, S. Jung, and J.-H. Park, "Viewing-angle-enhanced integral imaging using lens switching," *Opt. Lett.* **27**(10), 818–820 (2002).
23. S.-H. Hong, J.-S. Jang, and B. Javidi, "Three-dimensional volumetric object reconstruction using computational integral imaging," *Opt. Express* **12**(3), 483–491 (2004).
24. S.-W. Min, J. Kim, and B. Lee, "New characteristic equation of three-dimensional integral imaging system and its applications," *Japanese J. Appl. Phys.* **44**(2), L71–L74 (2005).
25. J.-H. Park, K. Hong, and B. Lee, "Recent progress in three-dimensional information processing based on integral imaging," *Appl. Opt.* **48**(34), H77-H94 (2009).
26. S. K. Nayar and V. N. Anand, "3D display using passive optical scatterers," *Computer* **40**(7), 54–63 (2007).
27. A. Sullivan, "3 Deep: new displays render images you can almost reach out and touch," *IEEE Spectrum* **42**(4), 30–35 (2005).
28. A. Jones, I. McDowall, H. Yamada, M. Bolas, and P. Debevec, "Rendering for an interactive 360° light field display," *ACM Trans.*

- Graph. **26**(3), 40 (2007).
29. S. Suyama, S. Ohtsuka, H. Takada, K. Uehira, and S. Sakai, "Apparent 3-D image perceived from luminance-modulated two 2-D images displayed at different depths," *Vision Res.* **44**(8), 785–793 (2004).
 30. Y. Kajiki, H. Yoshikawa, and T. Honda, "Hologram-like video images by 45-view stereoscopic display," *Proc. SPIE* **3012**, 154-166 (1997).
 31. T. Honda, D. Nagai, and M. Shimomatsu, "Development of 3-D display system by a fan-like array of projection optics," *Proc. SPIE* **4660**, 191-199 (2002).
 32. T. Balogh, P. Kovacs, and A. Barsi, "Holovizio 3D display system," in *Proceedings of 3DTV Conference 2007*, (Kos Island, Greece, 2007) 1–4.
 33. Y. Takaki and N. Nago, "Multi-projection of lenticular displays to construct a 256-view super multi-view display," *Opt. Express* **18**(9), 8824-8835 (2010)
 34. Y. Takaki and S. Uchida, "Table screen 360-degree three-dimensional display using a small array of high-speed projectors," *Opt. Express* **20**(8), 8848–8861 (2012).
 35. K. Nagano, A. Jones, J. Liu, J. Busch, X. Yu, M. Bolas, and P. Debevec, "An autostereoscopic projector array optimized for 3D facial display," in *ACM SIGGRAPH 2013*, (Anaheim, California, USA, 2013) 1.
 36. J.-H. Lee, J. Park, D. Nam, S. Y. Choi, D.-S. Park, and C. Y. Kim, "Optimal projector configuration design for 300-Mpixel multi-projection 3D display," *Opt. Express* **21**(22), 26820-26835 (2013).
 37. O. Cakmakci and J. Rolland, "Head-worn displays: a review," *J. Disp. Technol.* **2**(3), 199–216 (2006).

38. D. Cheng, Y. Wang, H. Hua, and M. M. Talha, "Design of an optical see-through head-mounted display with a low f-number and large field of view using a freeform prism," *Appl. Opt.* **48**(14), 2655–2668 (2009).
39. Y. Takaki and Y. Yamaguchi, "Flat-panel see-through three-dimensional display based on integral imaging," *Opt. Lett.* **40**(8), 1873–1876 (2015).
40. H. Hua and B. Javidi, "A 3D integral imaging optical see-through head-mounted display," *Opt. Express* **22**(11), 13484–13491 (2014).
41. H. J. Yeom, H. J. Kim, S. B. Kim, H. Zhang, B. Li, Y. M. Ji, S. H. Kim, and J. H. Park, "3D holographic head mounted display using holographic optical elements with astigmatism aberration compensation," *Opt. Express* **23**(25), 32025–32034 (2015).
42. Y. Takaki and Y. Yamaguchi, "Flat-panel see-through three-dimensional display based on integral imaging," *Opt. Lett.* **40**(8), 1873–1876 (2015).
43. F. Huang, K. Chen, and G. Wetzstein, "The light field stereoscope: immersive computer graphics via factored near-eye light field displays with focus cues," *ACM Trans. Graph.* **34**(4), 60 (2015).
44. R. Konrad, E. A. Cooper, and G. Wetzstein, "Novel optical configurations for virtual reality: evaluating user preference and performance with focus-tunable and monovision near-eye displays," in *Proc. of the ACM Conference on Human Factors in Computing Systems*, (San Jose, California, USA, 2016) 1211–1220.
45. C. C. Gordon, T. Churchill, C. E. Clauser, B. Bradtmiller, J. T. McConville, I. Tebbetts, and R.A. Walker, "Anthropometric survey of US army personnel: methods and summary statistics," United States Army Natick Research, Development, and Engineering Center, Natick,

MA (1988).

46. K. Akeley, S. J. Watt, A. R. Girshick, and M. S. Banks, “A stereo display prototype with multiple focal distances,” *ACM Trans. Graph.* **23**(3), 804–813 (2004).
47. S. Liu and H. Hua, “A systematic method for designing depth-fused multi-focal plane three-dimensional displays,” *Opt. Express* **18**(11), 11562–11573 (2010).
48. S. Ravikumar, K. Akeley, and M. S. Banks, “Creating effective focus cues in multi-plane 3D displays,” *Opt. Express* **19**(21), 20940–20952 (2011).
49. D. Teng, L. Liu, and B. Wang, “Super multi-view three-dimensional display through spatial-spectrum time-multiplexing of planar aligned OLED microdisplays,” *Opt. Express* **22**(25), 31448–31457 (2014).
50. S. Suyama, Y. Ishigure, H. Takada, K. Nakazawa, J. Hosohata, Y. Takao, and T. Fujikado, “Evaluation of visual fatigue in viewing a depth-fused 3-D display in comparison with a 2-D display,” *NTT Tech. Rev.* **3**(12), 82–89 (2005).
51. Y. Kim, H. Choi, J. Kim, S. W. Cho, Y. Kim, G. Park, and B. Lee, “Depth-enhanced integral imaging display system with electrically variable image planes using polymer-dispersed liquid-crystal layers,” *Appl. Opt.* **46**(18), 3766–3773 (2007).
52. X. Hu and H. Hua, “Design and assessment of a depth-fused multi-focal-plane display prototype,” *J. Disp. Technol.* **10**(4), 308–316 (2014).
53. S. Yoon, H. Baek, S. W. Min, S.-G. Park, M. K. Park, S. H. Yoo, H. R. Kim, and B. Lee, “Implementation of active-type Lamina 3D display

- system,” *Opt. Express* **23**(12), 15848–15856 (2015).
54. S. Liu, Y. Li, P. Zhou, X. Li, N. Rong, S. Huang, W. Lu, and Y. Su, “A multi-plane optical see-through head mounted display design for augmented reality applications,” *J. Soc. Inf. Disp.* **24**(4), 246-251 (2016).
 55. S.-G. Park, J.-Y. Hong, C.-K. Lee, M. Miranda, Y. Kim, and B. Lee, “Depth-expression characteristics of multi-projection 3D display systems,” *Appl. Opt.* **53**(27), G198-G208 (2014).
 56. Ricoh Co. Ltd., “Ultra short throw projectors,” <http://www.ricoh.com>.
 57. A. Travis, F. Payne, J. Zhong and J. Moore, “Flat panel display using projection within a wedge-shaped waveguide”, in *Conf. Rec. 20th Int. Display Res. Conf.*, (Palm Beach, Florida, USA, 2000) 292-295.
 58. A. R. L. Travis, T. Large, N. Emerton, and S. Bathiche, “Collimated light from a waveguide for a display backlight,” *Opt. Express* **17**(22), 19714–19719 (2009),
 59. M. Large, T. Large, and A. Travis, “Parallel optics in waveguide displays: a flat panel autostereoscopic display,” *J. Disp. Technol.* **6**(10), 431–437 (2010).
 60. A. R. L. Travis, T. A. Large, N. Emerton, and S. N. Bathiche, “Wedge optics in flat panel displays,” *Proc. IEEE* **101**(1), 45-60 (2013).
 61. S.-G. Park, C.-K. Lee, and B. Lee, “Compact multi-projection 3D display using a wedge prism,” *Proc. SPIE* **9391**, 939113-1 (2015).
 62. Y. K. Cheng, S. N. Chung, and J. L. Chern, “Aberration analysis of a wedge-plate display system,” *J. Opt. Soc. Am. A* **24**(8), 2357–2362 (2007).
 63. C.-K. Lee, T. Lee, H. Sung, and S.-W. Min, “Analysis and design of

- wedge projection display system based on ray retracing method,” *Appl. Opt.* **52**(17), 3964–3976 (2013).
64. Y. M. Kim, J. Yim, Y.-K. Ahn, and S.-W. Min, “Compensation of elemental image using multiple view vectors for off-axis integral floating system,” *Appl. Opt.* **53**(10), 1975-1982 (2014).
 65. Z. Zhang, “A flexible new technique for camera calibration,” *IEEE Trans. Pattern Anal. Mach. Intell.* **22**(11), 1330–1334 (2000).
 66. K. Hong, J. Hong, J.-H. Jung, J.-H. Park, and B. Lee, “Rectification of elemental image set and extraction of lens lattice by projective image transformation in integral imaging,” *Opt. Express* **18**(11), 12002-12016 (2010).
 67. Y. Takaki, “Super multi-view and holographic displays using MEMS devices,” *Displays* **37**, 19-24 (2015).
 68. K. Akşit, O. Eldeş, S. Viswanathan, M. Freeman, and H. Urey, “Portable 3D laser projector using mixed polarization technique,” *J. Disp. Technol.* **8**(10), 582-589 (2012).
 69. L. Liu, Z. Pang, and D. Teng, “Super multi-view three-dimensional display technique for portable devices,” *Opt. Express* **24**(5), 4421-4430 (2016).
 70. J.-H. Park, S. Jung, H. Choi, and B. Lee, “Integral imaging with multiple image planes using a birefringent crystal plate,” *Opt. Express* **11**(16), 1862-1875 (2003).
 71. Q.-X. Liu, W.-Z. Zhang, H.-F. Gao, and F.-H. Yu, “A new polarization multiplexing method for the micro LCOS projector optical system,” *Proc. SPIE* **7506**, 75061A (2009).

72. C.-K. Lee, S.-G. Park, J. Jeong, and B. Lee, "Multi-projection 3D display with dual projection system using birefringent crystal," *SID Symp. Dig. Tech. Pap.* **46**(1), 538-541 (2015).
73. J. Kim, Y. Kim, J. Hong, G. Park, K. Hong, S.-W. Min, and B. Lee, "A full-color anaglyph three-dimensional display system using active color filter glasses," *J. Inf. Disp.* **12**(1), 37-41 (2011).
74. A. Yariv and P. Yeh, *Optical Waves in Crystals* (Wiley, 1984), Chap. 4.
75. M. C. Simon and K. V. Gottschalk, "Waves and rays in uniaxial birefringent crystals," *Optik* **118**(10), 457-470 (2007).
76. M. Avendaño-Alejo, "Analysis of the refraction of the extraordinary ray in a plane-parallel birefringent plate with an arbitrary orientation of the optical axis," *Opt. Express* **13**(7), 2549-2555 (2005).
77. S. T. Lin, K. T. Lin and W. J. Syu, "Angular interferometer using calcite prism and rotating analyzer," *Opt. Commun.* **277**(2), 251-255 (2007)
78. A. J. Woods, "Crosstalk in stereoscopic displays: a review," *J. Electron. Imaging* **21**(4), 040902 (2012).
79. K. H. Lee, Y. Park, H. Lee, S. K. Yoon, and S. K. Kim, "Crosstalk reduction in auto-stereoscopic projection 3D display system," *Opt. Express* **20**(18), 19757-19768 (2012).
80. G. Wetzstein, D. Lanman, W. Heidrich, and R. Raskar, "Layered 3D: tomographic image synthesis for attenuation-based light field and high dynamic range displays," *ACM Trans. Graph.* **30**(4), 95 (2011).
81. D. Lanman, G. Wetzstein, M. Hirsch, W. Heidrich, and R. Raskar, "Polarization fields: dynamic light field display using multi-layer LCDs," *ACM Trans. Graph.* **30**(6), 186 (2011).

82. X. Hu and H. Hua, "High-resolution optical see-through multi-focal-plane head-mounted display using freeform optics," *Opt. Express* **22**(11), 13896–13903 (2014).
83. S. Moon, S.-G. Park, C.-K. Lee, J. Cho, S. Lee, and B. Lee, "Computational multi-projection display," *Opt. Express* **24**(8), 9025–9037 (2016).
84. S. Lee, C. Jang, S. Moon, J. Cho, and B. Lee, "Additive light field displays: realization of augmented reality with holographic optical elements," *ACM Trans. Graph.* **35**(4), 60 (2016).
85. G. D. Love, D. M. Hoffman, P. J. W. Hands, J. Gao, A. K. Kirby, and M. S. Banks, "High-speed switchable lens enables the development of a volumetric stereoscopic display," *Opt. Express* **17**(18), 15716–15725 (2009).
86. C. K. Park, S. S. Lee, Y. S. Hwang, "Depth-extended integral imaging system based on a birefringence lens array providing polarization switchable focal lengths," *Opt. Express* **17**(21), 19047–19054 (2009).
87. S.-G. Park, S. Yoon, J. Yeom, H. Baek, S.-W. Min, and B. Lee, "Lamina 3D display: projection-type depth-fused display using polarization-encoded depth information," *Opt. Express* **22**(21), 26162–26172 (2014).
88. H.-S. Chen, Y.-J. Wang, P.-J. Chen, and Y.-H. Lin, "Electrically adjustable location of a projected image in augmented reality via a liquid-crystal lens," *Opt. Express* **23**(22), 28154–28162 (2015).
89. Y. -H. Lee, F. Peng, and S. -T. Wu, "Fast-response switchable lens for 3D and wearable displays," *Opt. Express* **24**(2), 1668–1675 (2016).
90. J. Yeom, J. Jeong, C. Jang, K. Hong, S.-g. Park, and B. Lee, "Reflection-

- type integral imaging system using a diffuser holographic optical element,” *Opt. Express* **22**(24), 29617-29626 (2014).
91. C. Jang, K. Hong, J. Yeom, and B. Lee, “See-through integral imaging display using a resolution and fill factor-enhanced lens-array holographic optical element,” *Opt. Express* **22**(23), 27958-27967 (2014).
 92. K. Hong, J. Yeom, C. Jang, G. Li, J. Hong, and B. Lee, “Two-dimensional and three-dimensional transparent screens based on lens-array holographic optical elements,” *Opt. Express* **22**(12), 14363-14374 (2014).
 93. J. Yeom, K. Hong, Y. Jeong, C. Jang, and B. Lee, “Solution for pseudoscopic problem in integral imaging using phase-conjugated reconstruction of lens-array holographic optical elements,” *Opt. Express* **22**(11), 13659-13670 (2014).
 94. K. Hong, J. Yeom, C. Jang, J. Hong, and B. Lee, “Full-color lens-array holographic optical element for three-dimensional optical see-through augmented reality,” *Opt. Lett.* **39**(1), 127-130 (2014).
 95. C. Jang, C.-K. Lee, J. Jeong, G. Li, S. Lee, J. Yeom, K. Hong, and B. Lee, “Recent progress in see-through three-dimensional displays using holographic optical elements,” *Appl. Opt.* **55**(3), A71-A85 (2016).
 96. G. Li, D. Lee, Y. Jeong, J. Cho, and B. Lee, “Holographic display for see-through augmented reality using mirror-lens holographic optical element,” *Opt. Lett.* **41**(11), 2486-2489 (2016).
 97. M. Avendaño-Alejo and M. Rosete-Aguilar, “Optical path difference in a plane-parallel birefringent plate,” *J. Opt. Soc. Am. A* **23**(4), 926–932 (2006).

98. T. Mu, C. Zhang, Q. Li, L. Zhang, Y. Wei, and Q. Chen, "Achromatic Savart polariscope: choice of materials," *Opt. Express* **22**(5), 5043-5051 (2014).
99. J. Lesso, A. Duncan, W. Sibbett, and M. Padgett, "Aberrations introduced by a lens made from a birefringent material," *Appl. Opt.* **39**(4), 592–598 (2000).
100. D. Schmid, T.-Y. Huang, S. Hazrat, R. Dirks, O. Hosten, S. Quint, D. Thian, and P. G. Kwiat, "Adjustable and robust methods for polarization-dependent focusing," *Opt. Express* **21**(13), 15538-15552 (2013).
101. J. Wu, C. Zhang, Y. Zhang, H. Liu, and X. Zhai, "Refraction of extraordinary rays and ordinary rays in the Savart polariscope," *Chin. Phys. B* **17**(7), 2504–2508 (2008).
102. X. Chen, Y. Luo, J. Zhang, K. Jiang, J. B. Pendry, and S. Zhang, "Macroscopic invisibility cloaking of visible light," *Nat. Commun.* **2**, 176 (2011).
103. S. -G Park, J. -Y. Hong, C. -K. Lee, and B. Lee, "Real-mode depth-fused display with viewer tracking," *Opt. Express* **23**(20), 26710-26722 (2015).
104. D. Lanman and D. Luebke, "Near-eye light field displays," *ACM Trans. Graph.* **32**(6), 1-10 (2013).

Appendix

Portions of the work discussed in this dissertation are also presented in the following publications:

[Chapter 2] C.-K. Lee, S.-g. Park, S. Moon, J.-Y. Hong, and B. Lee, “Compact multi-projection 3D display system with light-guide projection,” *Opt. Express* **23**(22), 28945-28959, (2015).

[Chapter 3] C.-K. Lee, S.-g. Park, S. Moon, and B. Lee, “Viewing zone duplication of multi-projection 3D display system using birefringent crystal,” *Opt. Express*, **24**(8), 8458-8470, (2016).

[Chapter 4] C.-K. Lee, S. Moon, S. Lee, D. Yoo, J.-Y. Hong, and B. Lee, “Compact three-dimensional head-mounted display system with Savart plate,” *Opt. Express*, **24**(17), 19531-19544, (2016).

초 록

본 박사학위 논문에서는 광학적으로 투명한 매질에서의 광 경로 분석을 바탕으로 집약적인 3차원 디스플레이 시스템을 구현하는 접근 방법에 대하여 논의한다. 3차원 영상 장치를 구성하는 요소와 시청자 사이의 물리적인 거리를 줄이는 것은 집약적인 3차원 디스플레이 시스템을 구현하는 직관적인 방법이다. 또한, 기존 시스템의 크기를 유지하면서 더 많은 양의 3차원 영상 정보를 표현하는 것 또한 집약적 3차원 디스플레이 시스템을 의미한다. 높은 대역폭과 작은 구조를 가진 집약적 3차원 디스플레이 시스템을 구현하기 위하여 다음의 두 가지 광학 현상을 이용한다. 등방성 물질에서의 전반사 특성과 이방성 물질에서의 복굴절 특성이다. 가시광 영역에서 빛을 투과시키는 두 매질의 고유 광학 특성을 기존의 3차원 디스플레이 시스템에 적용하기 위하여 광 경로 추적을 통하여 분석한다.

광 도파로의 전반사 특성은 집약적 다중 투사 3차원 디스플레이 시스템을 구현하기 위하여 사용한다. 투사 광학계의 영상 정보는 광 도파로로 입사, 내부에서 전반사를 통하여 진행하고, 이에 수평 투사 거리는 광 도파로의 두께로 제한된다. 다수의 전반사 이후 영상 정보는 광 도파로의 출사 면을 통해 빠져나가고, 렌즈에 의하여 최적 시청 지점에서 시점을 형성한다. 광 도파로 내부에서의 광 경로를 등가 모델을 통하여 조사하고, 이를 통해 다수의 투사 광학계로부터 생성된 다수의 시점 영상이 왜곡되는 것을 분석하고 보정한다. 10개의 시점을 제공하는 집약적 다중 투사

3차원 디스플레이 시스템을 통해 제안된 방법을 검증한다.

향상된 대역폭 특성을 가진 다중 투사 3차원 디스플레이와 다중 초점 헤드 마운트 디스플레이 구현을 위한 이방성 판을 이용한 편광 다중화 방법을 제안한다. 빛의 편광 상태, 이방성 판의 광축 방향에 따라 광 경로가 달라진다. 측면 방향으로의 광 경로 전환은 다중 투사 3차원 디스플레이 기술과 결합하여 시점을 측면 방향으로 두 배로 증가시킨다. 깊이 방향으로의 광 경로 전환은 헤드 마운트 디스플레이에서 다중 초점 기능을 구현한다. 광 경로 추적 시뮬레이션을 통해 이방성 판의 모양, 광축, 파장 등의 다양한 파라미터 변화에 따른 광 경로 전환을 분석한다. 각각의 기능에 맞도록 설계된 이방성 판과 편광 회전자를 실시간으로 결합하여, 다중 투사 3차원 디스플레이와 다중 초점 헤드 마운트 디스플레이의 대역폭이 2배 증가한다. 각 시스템에 대한 시작품을 제작하고, 제안된 방법을 실험적으로 검증한다.

본 논문에서는 광 도파로와 복굴절 물질을 이용하여 그 광 경로를 분석, 대형의 다중 투사 3차원 디스플레이 시스템과 개인 사용자의 헤드 마운트 디스플레이 시스템의 크기를 감소시키고, 표현 가능한 정보량을 증가시키는 방법을 제안한다. 광 도파로와 이방성 판은 기존의 3차원 디스플레이 시스템과 쉽게 결합이 가능하며, 제안된 방법은 향후 소형뿐만 아니라 중대형 3차원 디스플레이 시스템의 집약화에 기여할 수 있을 것으로 기대된다.

주요어: 무안경식 3 차원 디스플레이, 전반사, 복굴절, 다시점 디스플레이, 편광 다중화, 헤드 마운트 디스플레이

학 번: 2013-30254